ARL-TR-7845 ● Oct 2016

US Army Research Laboratory

Structural Influence on the Mechanical Response of Adolescent Göttingen Porcine Cranial Bone

by Stephen L Alexander, C Allan Gunnarsson, and Tusit Weerasooriya

NOTICES

Disclaimers

The research reported in this document was performed in connection with contract W911-QX-14-C0016 and W911QX-16-D-0014 with the US Army Research Laboratory. The views and conclusions contained in this document are those of TKC Global Inc., SURVICE Engineering Company, and the US Army Research Laboratory.

The findings in this report are not to be construed as an official Department of the Army position unless so designated by other authorized documents.

Destroy this report when it is no longer needed. Do not return it to the originator.

ARL-TR-7845 ● OCT 2016

US Army Research Laboratory

Structural Influence on the Mechanical Response of Adolescent Göttingen Porcine Cranial Bone

by Stephen L Alexander
SURVICE Engineering Company, Weapons and Materials Directorate, ARL

C Allan Gunnarsson and Tusit Weerasooriya
Weapons and Materials Research Directorate, ARL

REPORT DOCUMENTATION PAGE

Form Approved
OMB No. 0704-0188

1. REPORT DATE *(DD-MM-YYYY)*	2. REPORT TYPE	3. DATES COVERED (From - To)
October 2016	Technical Report	April 2015–May 2016

4. TITLE AND SUBTITLE
Structural Influence on the Mechanical Response of Adolescent Göttingen Porcine Cranial Bone

5a. CONTRACT NUMBER

5b. GRANT NUMBER

5c. PROGRAM ELEMENT NUMBER

6. AUTHOR(S)
Stephen L Alexander, C Allan Gunnarsson, and Tusit Weerasooriya

5d. PROJECT NUMBER

5e. TASK NUMBER

5f. WORK UNIT NUMBER

7. PERFORMING ORGANIZATION NAME(S) AND ADDRESS(ES)
US Army Research Laboratory
ATTN: RDRL-WMP-B
Aberdeen Proving Ground, MD 21005-5069

8. PERFORMING ORGANIZATION REPORT NUMBER
ARL-TR-7845

9. SPONSORING/MONITORING AGENCY NAME(S) AND ADDRESS(ES)

10. SPONSOR/MONITOR'S ACRONYM(S)

11. SPONSOR/MONITOR'S REPORT NUMBER(S)

12. DISTRIBUTION/AVAILABILITY STATEMENT
Approved for public release; distribution is unlimited.

13. SUPPLEMENTARY NOTES
The research reported in this document was performed in connection with contract W911-QX-14-C0016 and W911QX-16-D-0014 with the US Army Research Laboratory. The views and conclusions contained in this document are those of TKC Global Inc., SURVICE Engineering Company, and the US Army Research Laboratory.

14. ABSTRACT
Bone specimens were dissected from the crania of adolescent Göttingen minipigs. These specimens were small cubes that contained the entire thickness of the skull. The microstructure of these skull specimens was quantified at the micron-length scale using micro-computed tomography (μCT). The skull microstructure demonstrated a clear porosity dependence on location along the skull thickness; the skull was highly porous near the skin-side surface and became less porous as location approached the brain-side surface. The skull specimens were then loaded in quasi-static compression to measure their mechanical response. The surface strain distribution on the specimen face was measured during loading using digital image correlation (DIC). The 2-D strain field formed a gradient of iso-strain bands along the thickness (depth) dimension from the skin-most to brain-most sides of the skull. The specimen was modeled by discretizing the depth dimension into a series of layers. The DIC measurements were then used to derive the stress-strain response of each layer. The initial portion of this response was used to calculate depth-dependent moduli for each layer. These localized mechanical properties were related with structural parameters calculated from the high-resolution images. The model enabled the prediction of local moduli based on morphological parameters measured with μCT and provided an estimation of the tissue modulus of the cranial bone.

15. SUBJECT TERMS
bone mechanics, cranial mechanics, skull morphology, minipig skull, DIC

16. SECURITY CLASSIFICATION OF:			17. LIMITATION OF ABSTRACT	18. NUMBER OF PAGES	19a. NAME OF RESPONSIBLE PERSON
a. REPORT	b. ABSTRACT	c. THIS PAGE			C Allan Gunnarsson
Unclassified	Unclassified	Unclassified	UU	94	19b. TELEPHONE NUMBER (Include area code) 410-306-0990

Contents

List of Figures

List of Tables

Acknowledgments

The authors would like to acknowledge the contributions of Ann Mae DiLeonardi (US Army Research Laboratory [ARL]) and Brett Sanborn (now at Sandia National Laboratories) for fabricating the bone compression specimens. The authors also acknowledge Michael Horsmon (Edgewood Chemical Biological Center) for providing the animal skulls with accompanying demographical data for these experiments. Finally, the authors would like to acknowledge the extensive technical feedback and comments of Adam Sokolow (ARL), which greatly improved the report.

1. Introduction

More than 235,000 US military service members were diagnosed with traumatic brain injury (TBI) from 2000 to 2011, and it is estimated that 1.7 million civilians sustain a TBI each year.[1] TBI incidence is associated with excessive external mechanical forces acting on the head. These applied forces effect inordinate strains in the hard and soft tissues of the skull and brain. Understanding the underlying mechanisms by which stresses and strains applied to these tissues induce TBI is crucial to designing head protection. An essential first step is to determine the thresholds of injury for the tissues of the head in response to mechanical loading.

In general, TBI studies that use impact and blast loading are conducted on animals rather than humans. However, the applicability of insight gained from nonhuman TBI impact and blast experiments relies on the ability to scale the animal injury thresholds to the human anatomy. The scaling relationship will depend on the mechanical response of the constituents of the human and animal head. The skull is particularly important since its mechanical response determines the transfer of deformation and stress to the brain during accelerative loading. The mechanical response of the skull, in turn, is dependent on its unique microstructure. Therefore, quantification of both the mechanics and morphology of the animal skull will enable any critical injury thresholds identified in an animal TBI study to be compared with and scaled to other species, including human.

Ongoing investigations at the US Army Research Laboratory (ARL) use the Göttingen minipig as a surrogate in impact experiments designed to better understand the mechanisms of TBI during mechanical loading. Both the mechanical response and the morphology of the skull have been previously studied in the human and large-breed pig, but this information is lacking for the minipig. In this report, the microstructure of cranial bone from adolescent (approximately 6 months old) Göttingen minipigs is quantified and related to the compressive response.

The macroscopic structure of the human cranium has previously been reported.[2,3] Mature human cranial bone is a sandwich structure of 3 layers with outer and inner tables composed of dense cortical bone.[2] The middle layer, the diploë, is porous trabecular bone. Generally, classification of bone tissue as cortical or trabecular is based on porosity.[3] Cortical (compact) bone is denser (porosity <30%), while trabecular (spongy) bone has higher porosity (>30%).

The degree of structural anisotropy in mature cranial human bone has also been characterized.[4,5] Some studies have classified cranial human bone as structurally isotropic, indicating that there is no prevailing directional bias in the arrangement of the bone. Dempster[4] punctured decalcified human skull away from the orbital cavities and facial structures to visualize the dominant direction of collagenous fibers in the outer table. He concluded that the fibers had a random orientation in the skull.[4] Similarly, McElhaney et al.[5] could not discern dominant directions in the histology of each of the 3 cranial layers. A lack of a dominant structural direction in cranial bone would be in sharp contrast to load-bearing bones, such as the femur. Previous studies at ARL have visualized the highly anisotropic structure of the femur, in which collagenous fibers are hierarchically arranged into lamellae, and the lamellae are predominately oriented in the loading direction.[6]

The microstructure of the skull evolves significantly with age, from birth to maturity. Both human and porcine cranial bones of newborns have a single layer of compact bone, with a separate porous layer formed with age.[7,8] Furthermore, young human cranial specimens have clearly identifiable grain patterns associated with fibrous orientation. These patterns make the immature specimens strongly anisotropic in contrast with the mature skull, which lacks such oriented structures.[9]

The mechanical response of human[5,10–14] and large-breed porcine[7,8] skulls has also been studied in various loading configurations. Margulies and Thibault[8] reported the modulus of human cranial bone tested in 3-point bending as increasing from approximately 800 MPa at 1 week of age to approximately 2.6 GPa at 6 months. Moduli from mature human crania tested in 3-point bending ranged from 3.28 ± 2 GPa[11] to 7.46 ± 5.39 GPa.[10] The mechanical response may become less dependent on bone orientation during maturation in conjunction with the loss of identifiable grain patterns. For example, the outer tables of mature specimens are only weakly anisotropic,[14–16] while the mechanical response of young specimens strongly depends on grain orientation.[17]

However, mechanical characterization of the cranium of the adolescent Göttingen minipig is lacking. The thickness and the microstructure of the minipig skull are known to significantly differ from that of the large-breed pig and are dependent on the weight of the animal. Large-breed pigs generally weigh more than 250 kg and their skull thickness ranges from 6 to 30 mm.[18] The mature Göttingen minipig weighs only 35–40 kg,[19,20] and its skull has proportionately larger frontal sinus cavities than large-breed pigs.[18] Previous human and large-breed porcine studies have shown that the mechanical response of the cranial bone is strongly dependent on its microstructure and that this structure changes significantly during maturation.[7–9] The microstructural differences between the minipig and the large-breed pig indicate that the existing mechanical response data from large-breed pigs

may not be adequate for use in computational models of minipigs or for correlation to the human. The differences therefore emphasize the need for the minipig skull to be independently characterized.

In this report the structure of the 6-month-old Göttingen minipig skull is quantified and related to its compressive mechanical response. Individual specimens were extracted from the skull for characterization of structure and mechanical response. The porosity and arrangement of the bone material within the specimen were quantified with micro-computed tomography (μCT). The mean intercept length (MIL) of the bone structure was obtained using μCT images to investigate the degree to which the cranial bone is structurally isotropic. Specimens were also loaded in the through-thickness (depth) direction, normal to the outer surface of the skull, at a quasi-static loading rate. The full-field strain tensor was measured using digital image correlation (DIC) while the specimen was loaded. Moduli at different depths were calculated from experimental measurements. These apparent moduli of the structure were related to the localized porosity measurement of the bone to determine the relationship between pure bone, the porosity percentage, and the apparent modulus. The relationship was used to predict the variation of modulus with depth.

2. Methods

2.1 Skull Specimen Extraction and Grouping

All specimens were extracted from Göttingen minipigs bred as part of an impact-based accelerative loading study at ARL. All procedures were approved by the ARL Safety Office and carried out in accordance with the rules and regulations of the Institutional Animal Care and Use Committee of the Edgewood Chemical and Biological Center. Three skulls were extracted from untested minipigs certified as originating from a US Department of Agriculture–licensed and –monitored herd and as having lived a healthy and disease-free life. Table 1 contains the age and weight information for these 3 pigs.

Table 1 Animal information

Skull no.	Age (weeks)	Weight (kg)	Sex
02	27.4	13	Male
03	25	13.2	Male
04	28	15.4	Male

Extraction followed procedures previously described[21,22] and illustrated in Fig. 1. Initially, specimens were taken from a region of extraction (ROE) of the skull. As shown in Fig. 1a, the ROE was located to avoid the large cavities located on the anterior aspect of the Göttingen minipig skull. Individual specimens were extracted from the ROEs for morphological and mechanical characterization and will be hereafter referred to simply as specimens. Using a diamond-coated bone pathology saw (Exact 312, Exact Technologies, Inc.), each specimen was cut through the thickness of the ROE normal to the surface so that external surface of the specimen was approximately a 4- × 4-mm square (Fig. 1b). The distance between these top and bottom surfaces, normal to the skin surface, will hereafter be referred to as the thickness or depth dimension. Generally, individual specimens were wet-sanded to roughly flat and parallel top and bottom surfaces prior to any morphological or mechanical characterization. A few specimens were also µCT-scanned prior to sanding (using the procedures described in the following) to understand sanding effects. Figure 2 shows the effects of sanding on one such specimen. Specimens were immersed in Hank's Balanced Salt Solution (HBSS) after extraction and sanding and stored at 4 °C until being used for µCT analysis and compression experiments.

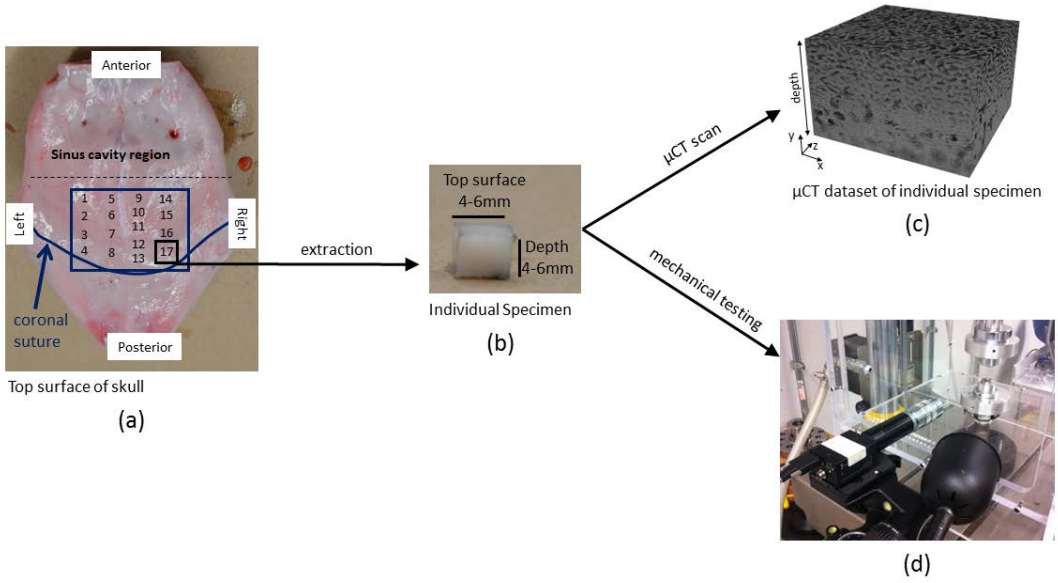

Fig. 1 Extraction of the individual specimens used for morphological and mechanical characterization

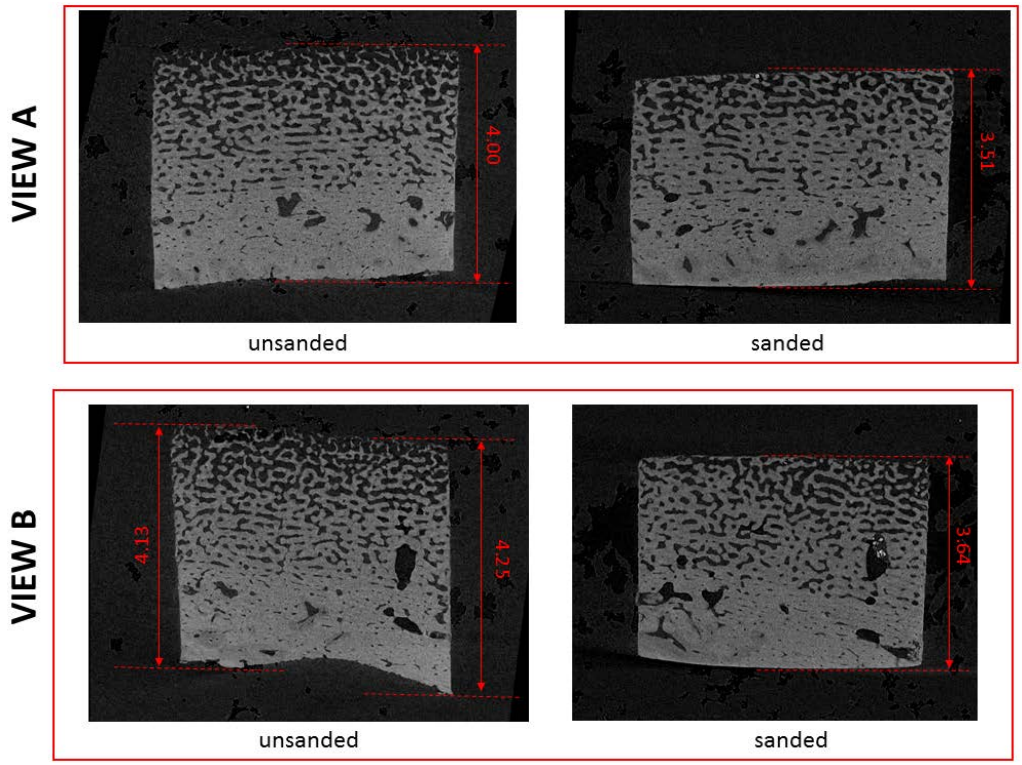

Fig. 2 Effect of sanding on Specimen 02-11

Individual specimens were labeled with the format *AA-BB*. The prefix *AA* identified the skull number as listed in Table 1: 02, 03, or 04. The suffix *BB* identified the individual specimen from each skull. Figure 1a contains an example of the *BB* numbering scheme used for Skull 02.

Preliminary mechanical tests used various specimens from the 3 skulls, and some of these results are described in the appendixes of this report. For the specimens described in this report, groupings were made on the basis of data availability and are not meant to be representative of all adolescent Göttingen minipigs. For example, some specimens had artifacts from the sanding process that rendered their µCT images unsuitable for quantitative analysis. In the following sections, a group of 14 specimens were used for statistics on morphology: 7 from Skull 02, 3 from Skull 03, and 4 from Skull 04. This group will be referred to as Group A. A subset of this group was used for direct mechanical-morphological analysis: specimens 02-07, 02-08, 02-11, and 02-15. This subset will be referred to as Subset A. Table 2 includes information for each of the specimens included in this report. The dimensions reported are of the specimens after sanding: length (l) and width (w) refer to the dimensions of the transverse plane parallel to the outer surface, and depth (d) refers to the distance from the outer to the inner surfaces.

Table 2 Specimens included in this report

Spec. name	Dimensions: l, w, d (mm)	Group A	Subset A	Mech. testing, other[a]	Density tests
02-07	5.19, 4.03, 4.14	X	X	. . .	X
02-08	5.07, 4.39, 5.38	X	X	. . .	. . .
02-09	4.89, 4.74, 6.07	X	. . .	. . .	. . .
02-10	5.28, 4.73, 4.28	X	. . .	Fig. 10	X
02-11	5.19, 4.68, 3.46	X	X	. . .	X
02-12	5.32, 4.80, 4.40	X	. . .	Fig. 10	. . .
02-15	5.67, 4.61, 5.08	X	X	. . .	X
03-01	5.30, 4.41, 5.21	. . .	. . .	Fig. 10	. . .
03-04	5.32, 4.73, 4.84	X	. . .	Fig. 10, Appendix B	X
03-05	5.16, 4.74, 6.38	X	. . .	Fig. 10, Appendix B	X
03-06	5.35, 4.92, 7.01	. . .	. . .	. . .	X
04-01	4.35, 3.96, 5.35	X	. . .	. . .	X
04-02	4.94, 3.95, 6.64	X	. . .	. . .	X
04-03	5.30, 3.80, 6.03	X	. . .	. . .	X
04-04	5.59, 4.94, 6.19	X	. . .	. . .	X

[a] These are other specimens, in addition to Subset A, that have mechanical data included in this report. The particular use of each specimen is listed.

2.2 Micro-Computed Tomography

The specimens were imaged prior to mechanical testing using a μCT scanner (Skyscan 1172, Bruker microCT) at 62 kV and 161 mA. The size of the isotropic voxel was 2.95 μm for all specimens except 02-11, for which the size was 2.82 μm. Specimens were wrapped in HBSS-saturated gauze to maintain hydration during imaging.

An image stack was reconstructed from the μCT data. The image stack sampled the depth dimension (*y* in Fig. 1c), with each image representing a slice of the specimen having a thickness of one voxel. The image plane will also be referred to as the transverse plane (*x*-*z* in Fig. 1c).

2.3 Compressive Mechanical Loading

Unconfined compressive loading was applied to individual specimens in the depth direction. This loading direction was shown as the *y* dimension in Fig. 1c, and the loading direction will be consistently referred to in this report as occurring in the *y* direction. The specimens were brought out of storage prior to compression, and one of the surfaces perpendicular to the loading platen was speckled for DIC. Specimens were loaded using an Instron servo-hydraulic load frame with a 5-kN load cell, as shown in Fig. 1d. The time between removal from storage and mechanical testing was minimized to reduce specimen dehydration and shape change. Generally, this time was kept below 30 min. The specimens were loaded under displacement control at an average nominal strain rate of 0.001/s, as determined from caliper measurements of the specimen thickness and controlled by the displacement of the Instron crosshead.

A charge coupled device camera (resolution = 1024 × 1024; frame rate = 1 Hz) coupled to a 2× magnification lens captured the 2-D deformation of the speckled plane during loading. Postprocessing software (VIC-2d 2009, Correlated Solutions) was used to calculate the 2-D displacements and strains from the deformation of the speckle pattern. The subset size used for correlations varied across specimens and was based on speckling and image quality. The sizes for Subset A were 99 px (529 μm) for Specimen 02-07, 55 px (294 μm) for Specimen 02-08, 99 px (529 μm) for Specimen 02-11, and 85 px (453 μm) for Specimen 02-15. Posttest image analysis of the speckles on specimens in Subset A indicated an approximate speckle size of 25 px (134 μm).

3. Results

3.1 Morphology

The μCT images were analyzed to calculate bone volume fraction and to describe the structural arrangement of the bone within the specimen. All analysis was performed using software provided by the CT manufacturer (Skyscan CT-Analyzer "CTan", Bruker microCT). Prior to any quantification, images were first binarized using an automated algorithm.[23]

3.1.1 Bone Volume Fraction and Apparent Density

Preliminary investigations indicated that the morphology of the specimens was highly gradient in the depth dimension from the inner surface (closest to the brain) to the outer surface (closest to the skin). The morphology showed little variation in the transverse direction. Appendix A contains additional data indicating that variation in the transverse plane was negligible relative to the large gradient in the depth dimension. Therefore, the bone volume fraction (BVF) was measured as a function of depth for the 14 specimens of Group A. First, the area ratio of bone to porous space was calculated for each binarized image. Figure 3a shows 2 example slices from an image stack in the depth dimension. The area ratio for a given image (depth) was assigned as the value of the BVF at that depth. This method was enabled by the fact that images had been reconstructed by averaging the depth (third) dimension over the voxel size. Therefore, each 2-D image actually contained information of the 3-D space.

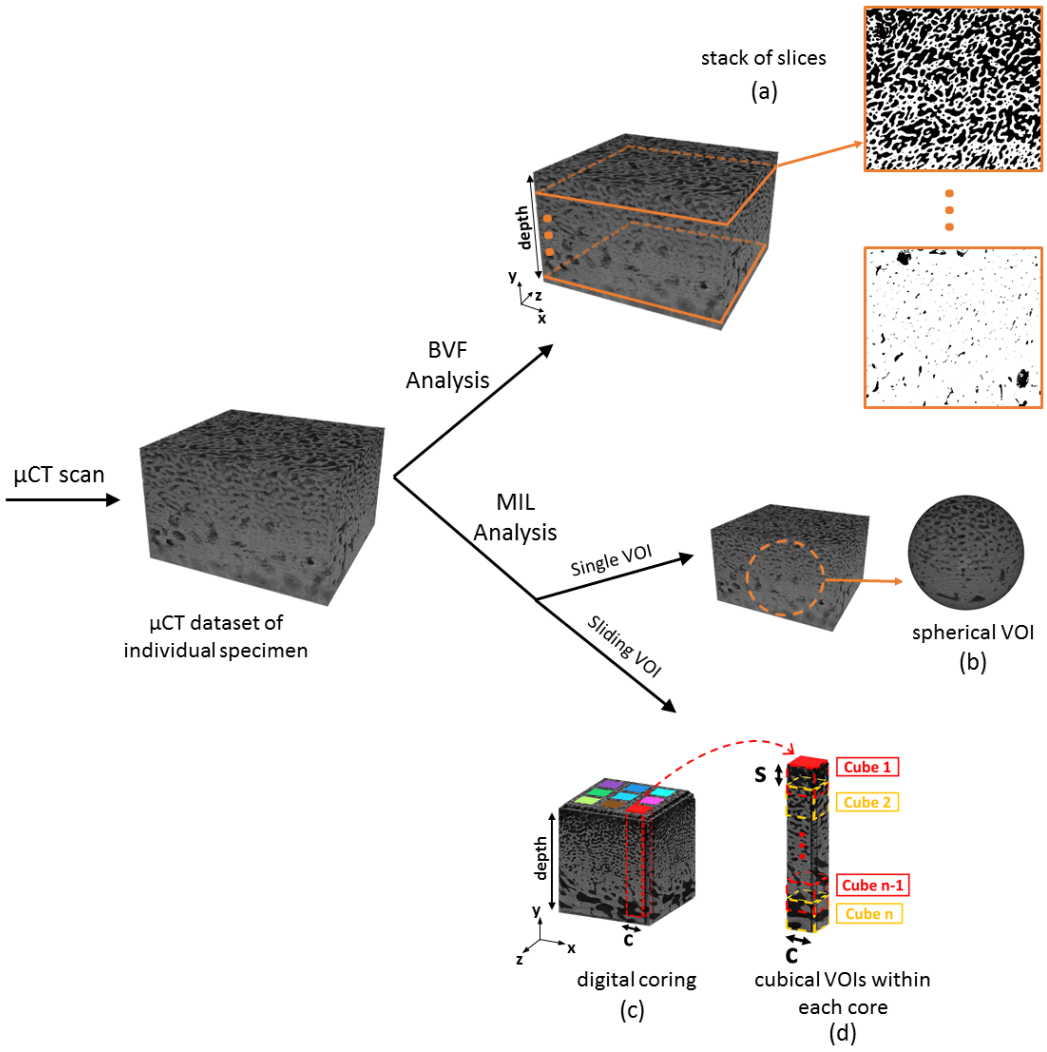

Fig. 3 Analysis of µCT data, including volume of interest (VOI)

Figure 4 shows the change of BVF with depth for the 4 specimens of Subset A. The BVF of each image was plotted as a function of depth percentage, ranging from 0% at the inner surface to 100% at the outer surface. The BVF results do not completely extend from 0% to 100% because data were not able to be extracted from images near the 2 extreme thickness values due to sanding artifacts. Figure 5 shows the BVF variation for all of Group A. In Fig. 5, the depth dimension was divided into 10 layers of equal thickness for compatibility with the mechanical modeling concept described in the following. For each skull, the data of all specimens were averaged over each layer since there was no repeatable intra-skull location-based variability. Specifically, the original in vivo location of the individual specimens within the skull ROE (shown for Skull 02 in Fig. 1a) did not have a discernable effect on bone volume trends.

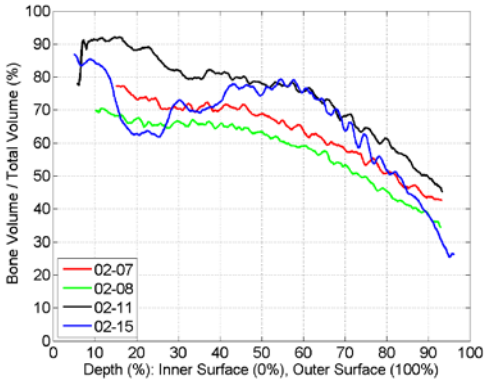

Fig. 4 BVF of each slice for the 4 specimens of Subset A, plotted as a function of thickness percentage

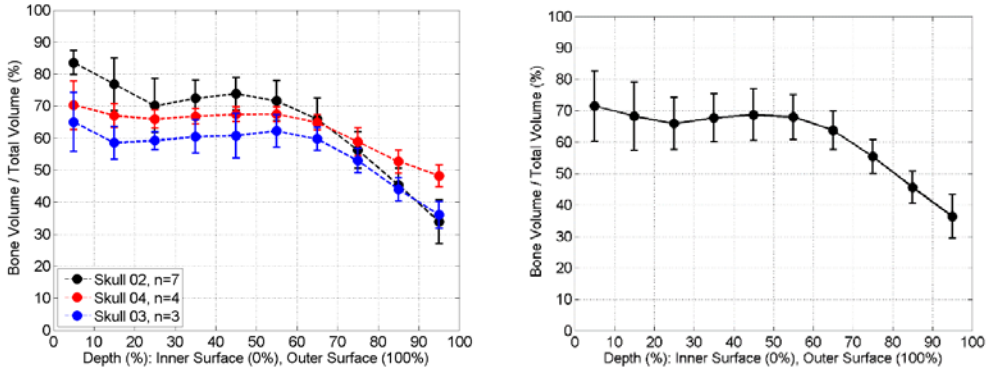

Fig. 5 BVF for all specimens of Group A

Apparent density was defined as the ratio of total mass to total volume of the specimen (sum of bones and pores): $\rho_a = m_t/V_t$. This is also the product of the density of the bone tissue, ρ_b, and the bone volume fraction, f_{bv}:

$$\rho_a = \rho_b f_{bv}. \quad (1)$$

To calculate the apparent density using Eq. 1, first the specimen-averaged bone tissue density, ρ_b, was experimentally measured. A group of 11 specimens (4 from Skull 02, 3 from Skull 03, and 4 from Skull 04) were removed from refrigeration and HBSS. The specimens were exposed to the laboratory atmosphere over several days for air-drying. During this time, periodic measurements were taken of the specimens' mass, using a digital scale (in milligrams), and volume, using digital calipers (in 100ths of 1 mm). The air-drying process was considered complete when no change (0%) in mass or the side lengths of the specimen were measured. Figure 6 shows the change in mass and volume during this air-drying period. At the end of this period, the bone tissue density of each specimen was then calculated as the ratio of the specimen's remaining mass to its volume (dried mass/dried volume), scaled by the average bone volume fraction of the whole specimen. The average bone tissue density was $\rho_b = 1.86 \pm 0.10$ g/cm^3.

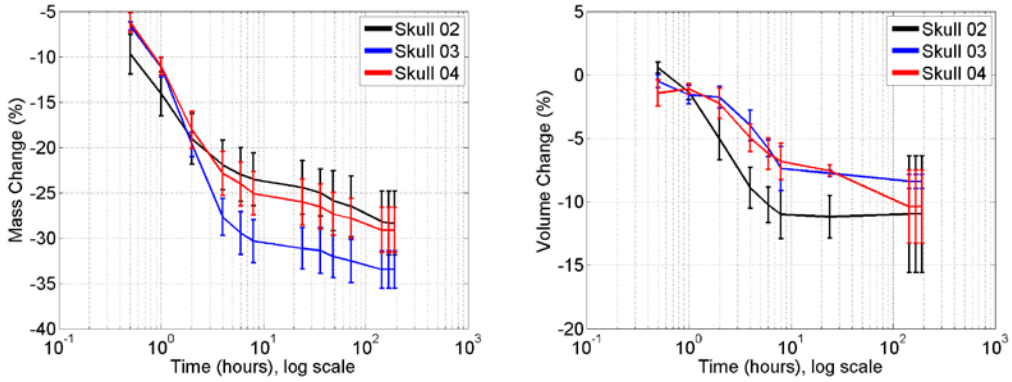

Fig. 6 Mass and volume changes during exposure to laboratory atmosphere

The depth-dependence of the BVF in Group A (Fig. 5) was then multiplied by the measured ρ_b to calculate a prediction of the change of apparent density with depth. Figure 7 shows the depth-dependent apparent density.

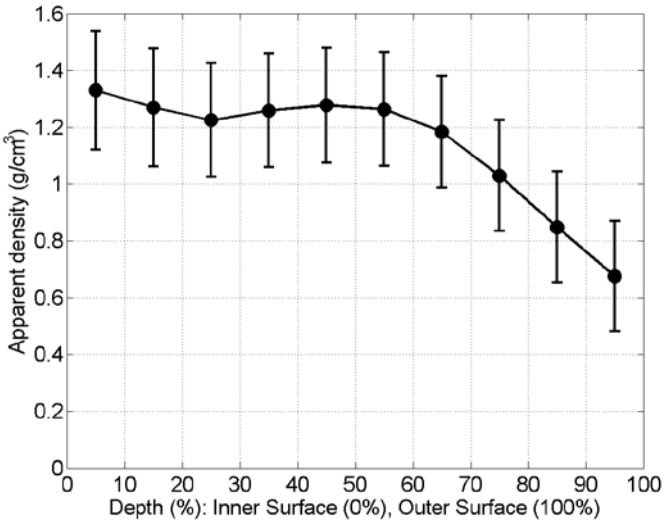

Fig. 7 Predicted change of apparent density with depth for Group A

3.1.2 Structural Arrangement

The structural arrangement of the bone phase within the individual specimen was also quantified using the µCT datasets of the specimens in Subset A. First, VOIs were extracted from each specimen's µCT dataset, as described in the following. The components of the MIL tensor[24] were then calculated over each VOI. The principal axes of the MIL tensor are related to the principal axes of the bone phase averaged over the VOI.[24] The MIL analysis was performed using the CT-Analyzer software (grid spacing of 25 µm, 1024 tested orientations).

Two different types of VOIs were extracted from each specimen's μCT dataset for subsequent MIL analysis, as was shown in Fig. 3. A single spherical VOI was extracted from the centroid of the μCT dataset to describe the average arrangement over the whole specimen (Fig. 3b). The diameter of the sphere was constrained by the smallest dimension of the specimen's μCT dataset in order for the sphere to be completely contained within the dataset.

In addition, a "sliding VOI" methodology was implemented to quantify the spatial variation of the structural arrangement in both the depth dimension and across the transverse plane. For this method, an array of 9 squares was created at the outermost image slice, each with a side length c (Fig. 3c). Digital cores were then created from each of these squares by sweeping through the image stack from the outermost to the innermost image. An example core is shown in Fig. 3d. In each core, the image stack consisted of cross-sectional images in the transverse plane of dimension $c \times c$. The depth dimension of each core, shown as the y dimension in Fig. 3d, was subdivided into a number of cubical VOIs. The top surfaces of the cubical VOIs were separated by a length s, where $s < c$. Therefore, calculation of morphological parameters within each cubical VOI provided a moving average in the depth dimension. This moving average method was inspired by a similar technique that others have used to quantify the complex trabecular orientation of the calcaneus.[25]

In this study, the parameters c and s were independently set for each specimen to satisfy 2 constraints based on specimen dimensions and the researcher's qualitative assessment of the specimen's morphology. First, the depth dimension (d) of each core was sampled by 10–13 cubical VOIs to adequately quantify depth-dependent changes. The total number (n) of cubical VOIs created to sample the entirety of d was specified as $n = ((d - c)/s) + 1$. Second, the cubical VOI needed to be sufficiently large to contain multiple trabecular crossings in order for the MIL analysis to provide meaningful results.[26] To satisfy these constraints, the cube size (c) was set to about 25% of the total depth (d) dimension. The shifting parameter (s) ranged between 80 and 90 μm.

Figures 8 and 9 show the results of the MIL analysis for Subset A, with subsets in each subfigure showing the location of the cores on the outermost image slice (x-z plane). Core location generally followed a grid layout so that the transverse plane (x-z) was adequately sampled. Deviations from the grid were made to avoid artifacts in the CT dataset, such as sanding particles.

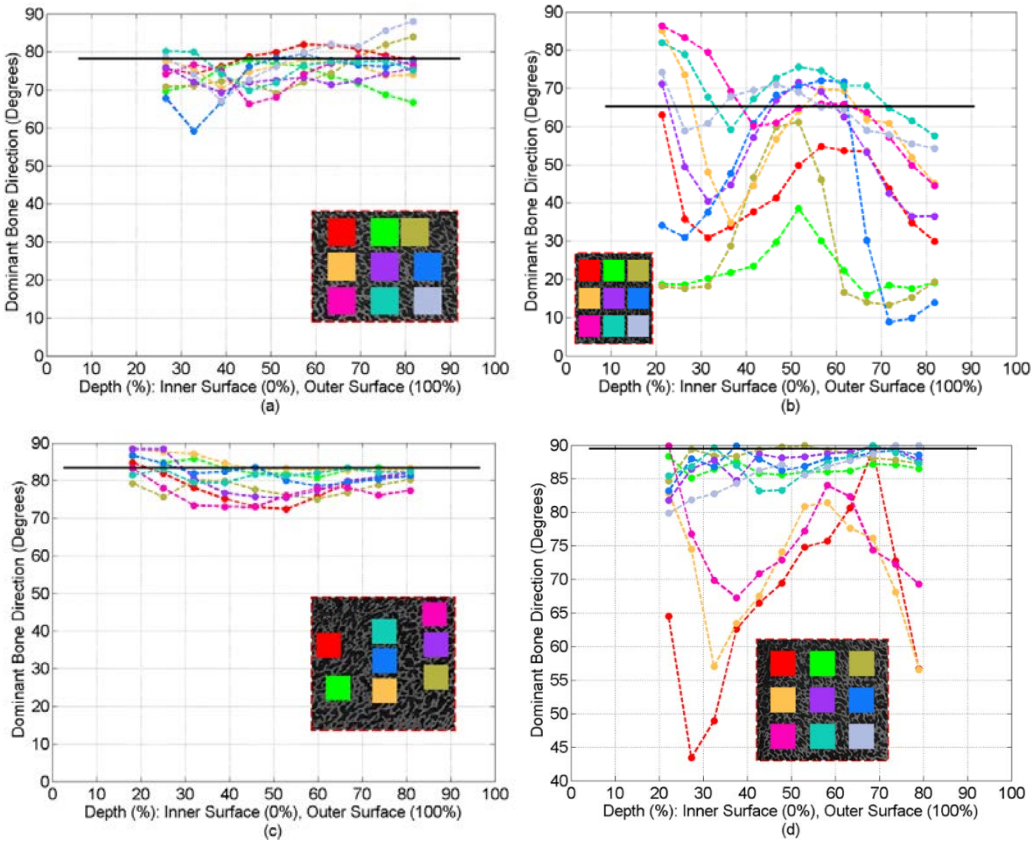

Fig. 8 Results of MIL analysis for Subset A: bone orientation

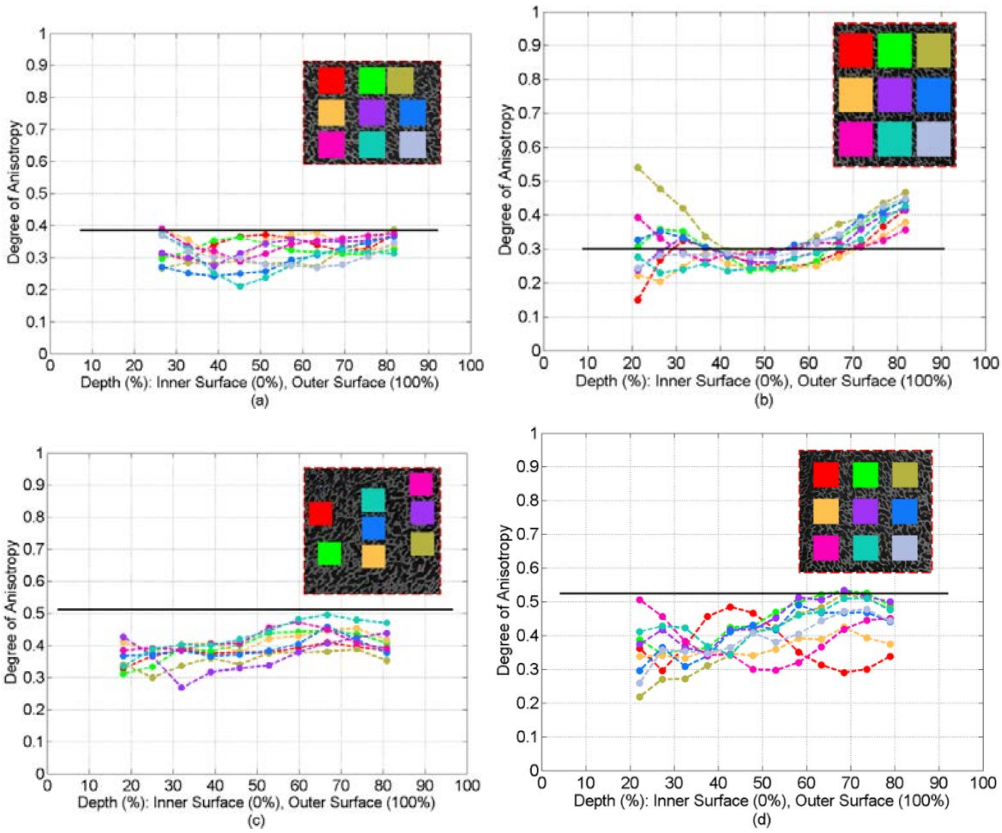

Fig. 9 Results of MIL analysis for Subset A: degree of anisotropy (DA)

The dominant bone direction was defined by the eigenvector of the MIL tensor with the smallest eigenvalue. The orientation angles shown in Fig. 8 were then calculated as the angle between this dominant bone direction and the compression loading direction. The DA shown in Fig. 9 was calculated by first finding the ratio of the smallest eigenvalue, λ_1, to the largest eigenvalue, λ_3, of the MIL tensor. This ratio was then subtracted from 1: $DA = 1 - \lambda_1/\lambda_3$. This DA calculation provided results that ranged from the perfectly isotropic case of 0 to the perfectly anisotropic case of 1. Many alternative methods of defining DA exist, but this method was used for comparison with values calculated by other programs such as BoneJ.[27]

The MIL tensor results of Figs. 8 and 9 motivated the subsequent treatment of the cranial specimens as isotropic. For example, the structural arrangement did not show a clearly defined spatial variation. No repeatable trend of depth-dependence was exhibited, contrary to the trend seen in the BVF (Figs. 4 and 5). Moreover, trends were not repeatable from specimen to specimen, again in sharp contrast to the BVF. The average DA of the cubical VOIs from the sliding VOI method was 0.35 ± 0.07. This is low (more isotropic) compared with other anatomic sites that contain low-BVF bone. For example Prot et al. reported trabecular bone specimens from bovine femurs to have a DA of 0.53 ± 0.08.[28]

3.2 Compressive Mechanical Response

The apparent far-field stress-strain response is shown in Fig. 10 for a sample of specimens that were mechanically loaded. This response was measured as a first-order attempt to inform further analysis. The stress was calculated by normalizing the load cell force by the undeformed cross-sectional area of the specimen, as measured with digital calipers. The strain shown in Fig. 10 is engineering strain calculated using displacement measured from the Instron load frame. These methods of calculating stress from the load cell and strain from the machine displacement provided the macroscopic response of the entire specimen. This far-field response will be referred to in this report as the *apparent* stress-strain response.

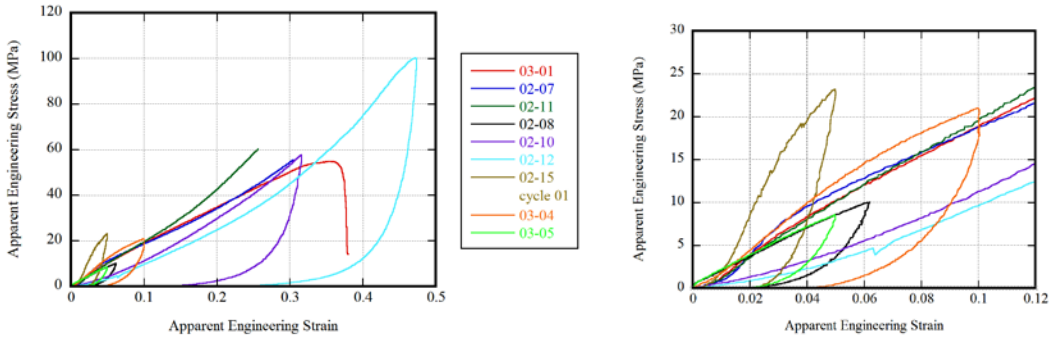

Fig. 10 Apparent stress-strain responses of a sample of specimens loaded in quasi-static compression

Specimen 02-15 was compressed several times to examine the repeatability of the small-strain response. The specimen was quasi-statically loaded to 5% apparent strain as measured from the machine displacement. It was then unloaded at the same quasi-static rate and allowed to recover for 30 min before another loading cycle was applied. Figure 11 shows the apparent stress-strain response for 2 load-unload cycles. Elastic moduli remained relatively constant between the first cycle, 577 MPa, and the second cycle, 702 MPa. Appendix B contains the results of other specimens and methods used to investigate the issue of elastic recovery. Figure 12 shows contours of the DIC-derived localized strain for Specimen 02-15. Strain is in the loading direction (y) and taken at the time corresponding to maximum load. Contours showed that the depth dimension of the strain field was roughly divided into several horizontal (x dimension) bands of strain.

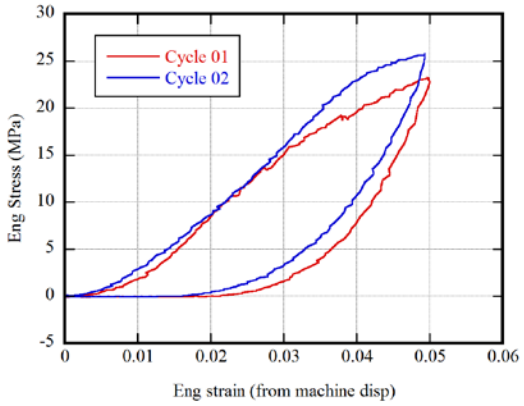

Fig. 11 The 2 load-unload cycles of Specimen 02-15. Cycles were separated by a 30-min recovery period.

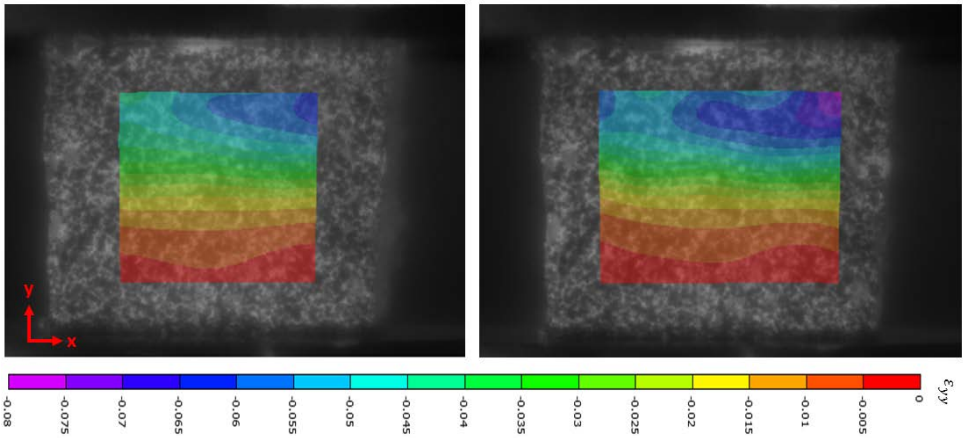

Fig. 12 DIC-derived contours of the strain in the compression direction (ε_{yy}) for Specimen 02-15

3.3 Relating Morphology to Mechanics

The strain bands observed in the DIC results indicated that the functional gradient of the morphology, as seen in the BVF (Figs. 4 and 5), was effecting a gradient in the mechanical response. Therefore, the individual specimens of Subset A were mechanically modeled by discretizing the depth dimension into 10 layers acting in series. The modeling framework is shown schematically in Fig. 13. For each layer, the morphology was approximated as constant with a single BVF value, f_{BV}^{n}. This single BVF value of the layer was calculated by averaging the depth-dependent BVF over the spatial area of the layer.

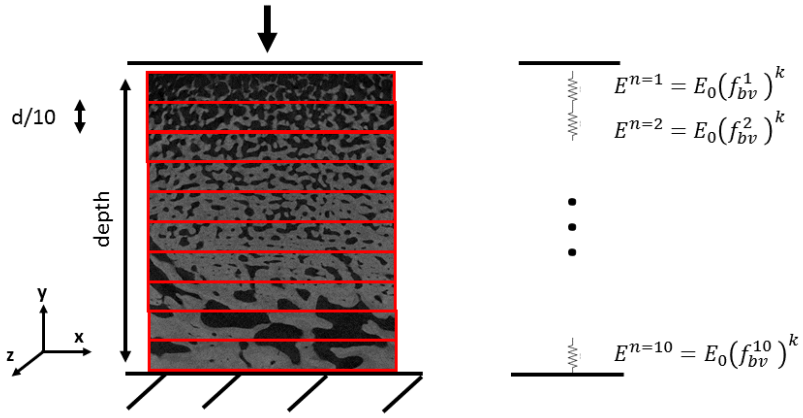

Fig. 13 Schematics showing the modeling framework

Each layer was modeled as also having a single apparent modulus, E^n. The layer's apparent modulus was derived by scaling the tissue modulus, E_0, of the bone phase (BVF = 1) by a power of the layer's average BVF:

$$E^n = E_0(f_{BV}^n)^k. \quad (2)$$

3.3.1 Fitting the Model Parameters

Two parameters from Eq. 2 were experimentally derived, E^n and f_{BV}^n, and 2 parameters were found through fitting to results, E_0 and *k*. The average BVF value of each layer, f_{BV}^n, was directly calculated from the μCT data, as shown in Fig. 5. The layer's apparent modulus, E^n, was derived from the compression loading results in the following manner. First, the strain in the loading direction, ε_{yy}, was obtained for each time point of the experiment from postprocessing of the DIC data (Vic-2D 2009, Correlated Solutions Inc., Columbia, South Carolina). The strain at any given time point was a function of the *x*-*y* position across the speckled face. The average strain of each layer, ε_{yy}^n, was defined by averaging ε_{yy} over the *x*-*y* area of the layer. Repeating this procedure for each time point in the test produced the evolution of layer-specific strain with time, $\varepsilon_{yy}^n(t)$.

Compressive stress in the loading direction, $\sigma_{yy}(t)$, was calculated by normalizing the load from the load cell by the nominal cross-sectional area of the specimen (apparent stress, as in Section 3.2). This calculation was also set as the stress of each layer, $\sigma_{yy}^n(t) = \sigma_{yy}(t)$, since the layers of the specimen were modeled as acting in series.

Finally, the stress-strain response of each layer was obtained by matching the time domains of $\sigma_{yy}^n(t)$ and $\varepsilon_{yy}^n(t)$. A linear regression of the initial portion of this stress-strain response was performed to calculate the apparent elastic modulus of the layer, E^n. Figure 14 provides a schematic example of the process of obtaining the stress-strain response of the layers and their moduli, E^n.

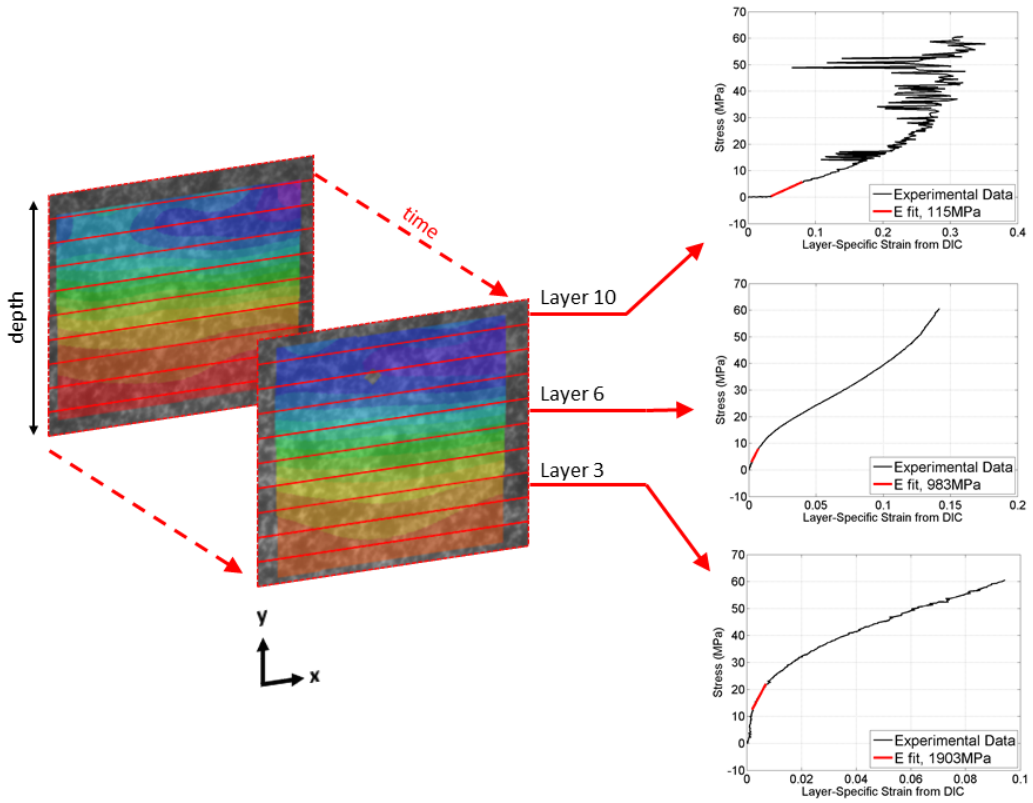

Fig. 14 Schematic showing the derivation of the stress-strain response of each layer

From the 4 specimens of Subset A, the apparent elastic modulus was calculated for a total of 32 layers. There were a total of 8 layers for which an initial, linear stress-strain response was not discernible. These layers were therefore not included in further analysis. Appendix C contains data relating to the linear regression performed on the 32 layers to derive the elastic modulus of the layer. Appendix C also includes the stress-strain response of each layer and compares the evolution of the layer-averaged shear strain, $\varepsilon_{xy}^{n}(t)$, to the normal strain, $\varepsilon_{yy}^{n}(t)$. The shear strain was generally negligible. The shear strain did not monotonically increase with increased loads as did the normal strain. Furthermore, the modulus was generally calculated from time points for which the ratio of shear strain to normal strain, $\varepsilon_{xy}^{n}(t)/\varepsilon_{yy}^{n}(t)$, was less than roughly 0.25 (shown in Appendix C.)

The solid markers of Fig. 15 show the apparent modulus of each layer (E^n) as a function of the layer's average BVF, f_{BV}^{n}. Figure 16 provides an example schematic of how one of the data points was derived using the procedure outlined previously.

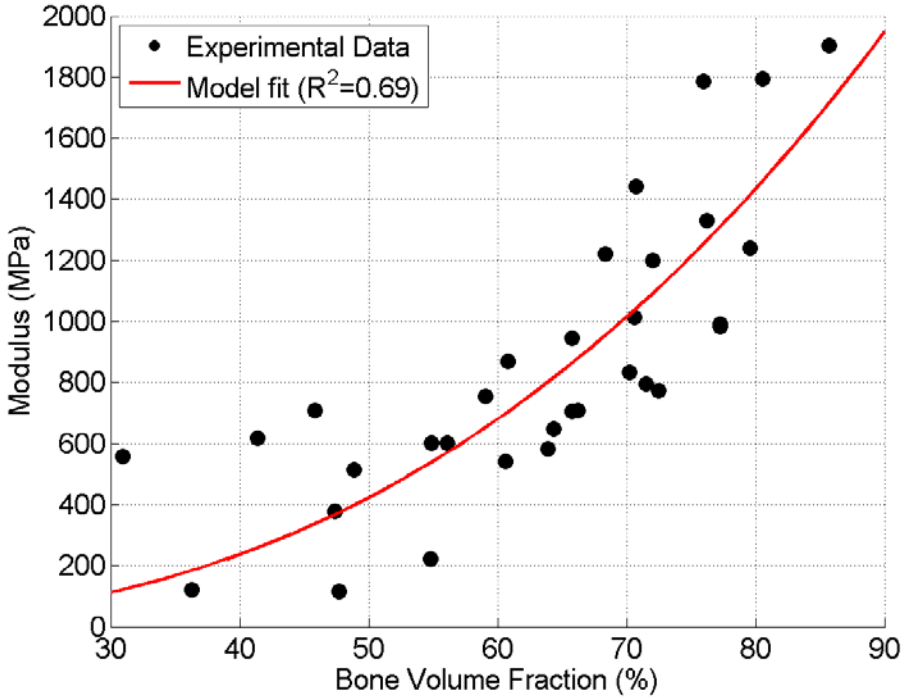

Fig. 15 Modulus of each layer plotted as a function of the layer's average value of BVF

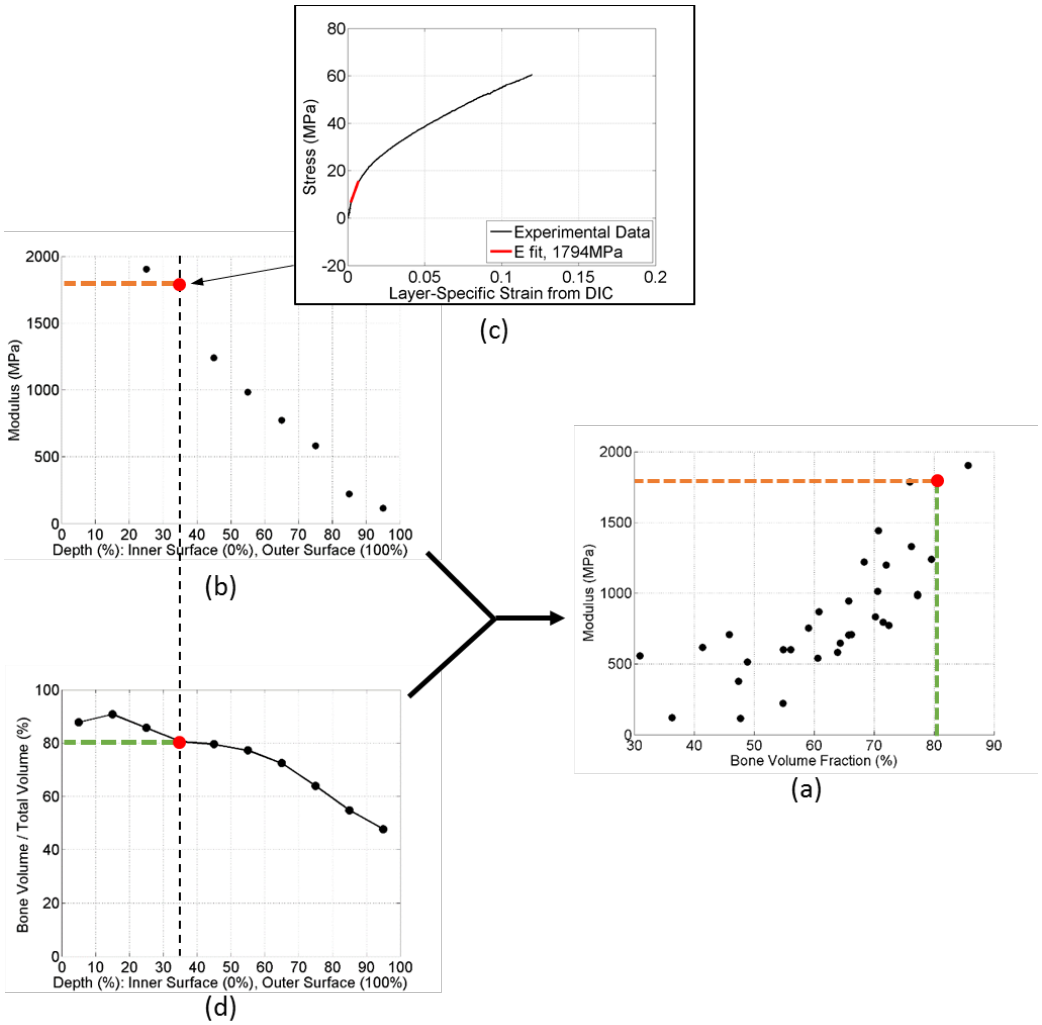

Fig. 16 Example of the derivation of the modulus-BVF experimental results shown in Fig. 15

Equation 2 was then calibrated by fitting 2 parameters to the experimental data of Fig. 15: the tissue modulus, E_0, and the BVF scaling parameter, k. The tissue modulus was assumed to be a constant material property of the bone phase. The scaling parameter k was assumed to be constant for all layers. Therefore, the variation of the modulus with depth was modeled as solely due to the variation of the bone volume fraction with depth, as depicted in the schematic of Fig. 13. A nonlinear least squares method (MATLAB) was used to fit the power relationship of Eq. 2, and the results are also shown in Fig. 15. The resulting parameters, with a 95% confidence interval, were E_0 = 2562 MPa (1865,3259) and k = 2.60 (1.82,3.38). The resulting fit for Eq. 2 was, therefore,

$$E^n = 2562(f_{BV}^n)^{2.60}. \quad (3)$$

3.4 Estimating the Variation in Mechanical Properties

Equation 3 described the relationship between each layer's average BVF and the layer's apparent modulus as fit from Subset A. The relationship was assumed to be valid for all of the specimens of Group A as a first-order approximation. Therefore, Eq. 3 was used to make an estimation of the depth-dependence of the apparent modulus for all specimens of Group A. The apparent moduli of these specimens were calculated by using Eq. 3, with f_{BV}^{n} taken from the statistics of the layer-averaged BVF for Group A (Fig. 5). The result is shown in Fig. 17. The modulus is predicted to drop by almost an order of magnitude, on average, from the outermost layer (1.1 GPa) to the innermost layer (200 MPa). A single through-thickness modulus was also derived using the approximation that the layers act in series. The iso-stress limit yields an average through-thickness modulus of 563 MPa. Application of this limit to the upper and lower standard deviations shown in Fig. 17 results in through-thickness moduli of 762 and 351 MPa.

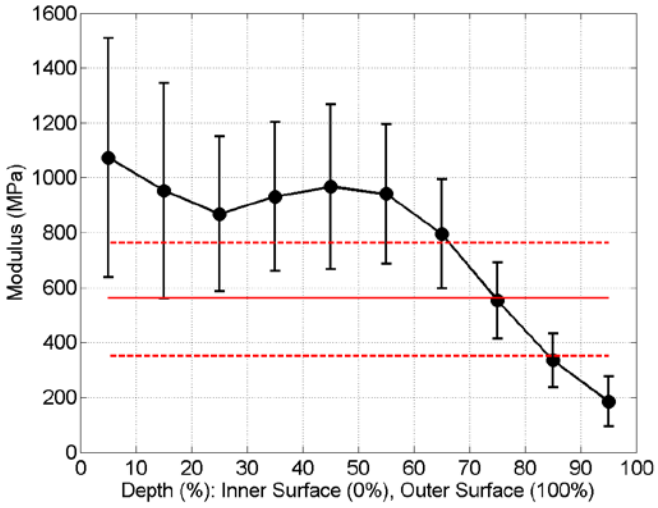

Fig. 17 The predicted variation of modulus (mean ± std) with depth for all specimens within Group A

4. Discussion

This study characterized the morphology of the adolescent minipig cranium and measured its mechanical response to quasi-static compression. The models obtained from this study can be directly used in finite element models to improve the biofidelity of the simulation. Computational limitations restrict the amount of detail, such as pore structure, that can be accurately represented in the mesh. As a result, solid elements often represent portions of the skull that are actually porous. Assigning microstructurally inspired material models for these elements, which

intrinsically account for the biphasic mixture, would greatly improve the biofidelity of the model over simply using parameters derived for pure bone. For example, the apparent density, by its definition (Eq. 1), can be directly assigned as the density of an element representing a biphasic mixture of bone and porous space. The modulus of these biphasic elements in the linear elastic approximation can also be derived from the apparent modulus reported as a function of depth (Fig. 17). The limitations of these results are discussed in the following, as well as their comparison with previous cranial bone studies.

4.1 Morphology

4.1.1 Depth Dependence of BVF and Apparent Density

The adolescent minipig skull had denser bone along the inner surface that gradually transitioned to an extremely fine, porous structure at the outer surface. The BVF changed by almost a factor of 2 from one surface to the other: from an average BVF at the inner surface of 71% to a BVF at the outer surface of 38%. On average, this transition occurred at a depth of slightly more than 50% of the thickness. The BVF transition was accompanied by a decrease in the apparent density from ρ_a = 1.32 ± 0.21 g/cm^3 at the inner surface to ρ_a = 0.66 ± 0.22 g/cm^3 at the outer surface. The apparent density results correlated with ranges found in human bone. The apparent density averages 1.8 g/cm^3 in human cortical bone and from 0.1 to 1.0 g/cm^3 for human trabecular bone.[3] Moreover, the present results for bone tissue density, ρ_b = 1.858 ± 0.104 g/cm^3, were closely related to the density of the outer table of the human skull's parietal (1.812 ± 0.127) and frontal (1.783 ± 0.128) bones.[14] The bone tissue density results were meant to approximate the density of the bone material (BVF = 100%). Therefore, they should be comparable to results reported elsewhere for dense cortical bone, the type of bone in the outer table of the human skull.

However, the transition in bone type found in the developing minipig skull differed significantly from previous reports on cranial architecture. First, the 2 types of bone did not form the distinct layers typical of the mature human skull. The transition was gradual rather than sharp. Furthermore, previous human and large-breed porcine studies reported the denser layer positioned toward the outer surface. The transition in bone type found in the adolescent minipig of the present study was in the opposite direction, with denser bone positioned toward the inner surface and more porous bone toward the outer surface.

The differences between adolescent and mature crania may be partly due to structural changes associated with the maturation of the minipig, since skull morphology is known to profoundly evolve during development. For example, the

skulls of infant human and large-breed pigs have structures that are different from their adult counterparts and which rapidly evolve during development. While adult human and domestic pig skulls have distinct cortical and trabecular layers,[7] the skull of large-breed pigs aged only a few days is almost entirely cortical bone.[8] Differentiation of the skull into distinct layers of trabecular and cortical bone was only observed at 25 days of age in pigs[7] and during the first 6 months after birth in humans.[8] On the other hand, the differences between the present results and previous studies could also be due to the use of high resolution (~3 μm) or to the limited sample size (3 skulls) of the present study. For example, μCT scans at a lower resolution of 50 μm of the same type of cranial bone (same breed and general age as the present study) were previously carried out as part of ongoing work at ARL.[29] These scans gave the incorrect perception that the outer layer was denser than the inner layer, likely due to the use of a scanning resolution that was almost 17-fold less refined than that of the present report.

4.1.2 Structural Isotropy

The structural arrangement was quantified by measuring the DA and the dominant orientation of the bone relative to the loading axis. The spatially dependent results of both the DA and the orientation indicated that the bone specimens could be approximated as structurally isotropic at length scales investigated in this report. First, the average DA (0.35 ± 0.07) was lower than that reported in the femur.[28] Furthermore, the overall change of bone orientation with depth was not repeatable between specimens and was on the same order of magnitude as the variation across the transverse plane (Fig. 8). This spatial variation of bone orientation was in sharp contrast to the spatial variation of the BVF. The BVF showed a repeatable trend of depth-dependence observed in all specimens, and there was more change in the depth direction than across the transverse plane.

The approximation of cranial bone as structurally isotropic at the length scale of the whole specimen had also been made in earlier studies conducted on the human skull. For example, Dempster[4] punctured decalcified human skulls to visualize fiber orientation in the outer table. A random orientation of these punctured "split lines" were seen in regions posterior to the orbital cavities. However, the split line technique only investigated orientation effects on the outer table. McElhaney et al.[5] examined the histology of all 3 layers of the human skull and reported a seemingly random orientation with no preferred direction.

4.1.3 Limitations of Morphology Measurements

The sliding VOI method was used to study the spatial variation of the bone orientation and DA using an overlapping, moving average in the depth dimension.

Therefore, local variations in the depth-dependency of the structure over a length scale much smaller than the size of the cubical VOIs (~1/4 of the thickness) were not fully captured. Furthermore, the variation in morphology across the transverse plane was also not completely captured by the limited number of cores extracted from each specimen. As an example, the cores of Specimen 02-11 covered approximately 40% of the transverse area.

However, the moving average technique using overlapping VOIs was necessary to investigate spatial variation while balancing the requirements of the MIL analysis. This analysis reports the fit (of an ellipsoid) to an averaged parameter (the mean of the intercept lengths). As a result, MIL requires the VOI to be sufficiently large to contain multiple trabeculae and pores[26] to avoid filtering out nuances in the data. Therefore, the depth-dependence would have only been investigated with a small number of non-overlapping VOIs, limiting the insight into spatial variation.

The single VOI method was also used to measure the average bone orientation over the whole of the specimen. The VOI was centered in the middle of the specimen. Therefore, the results were biased toward the center of the specimen, and information toward the extreme inner and outer surfaces was lost. In Figs. 8 and 9, the depth-independent black lines are the results of the single VOI method, and the depth-dependent colored lines are the results from the sliding VOI method. A simple comparison of these results indicates that the single VOI may be an insufficient measure of the morphology.

4.2 Mechanical Properties

The power law of $E^n = 2562(f_{BV}^n)^{2.60}$ (Eq. 3) related the apparent modulus (E^n) of a localized portion of the specimen to both the localized BVF and to the tissue modulus of solid bone having a BVF of 1.0. The literature contains many uses of a similar type of power law relationship between the apparent modulus of trabecular bone and its density, as reviewed by Helgason et al.[32] However, this type of relationship has generally been used to relate the through-thickness modulus of a specimen to the specimen-averaged density. In the present study, the power law was used to relate localized (depth-dependent) changes in modulus to the local morphology within individual specimens.

Several factors should be considered when comparing the power relationship of Eq. 3 with results reported in the literature. Most studies reporting a similar type of power relationship investigated bone from anatomical sites other than the skull. Inter-site correlation is difficult since the power relationship between BVF and apparent modulus has been found to be highly sensitive to anatomic site.[32,33]

However, the scaling parameter k = 2.60 is an exception for which comparison of results with those of other studies may be possible. First, this exponential parameter remains insensitive to whether the apparent modulus, material density, or BVF is used to scale the bone tissue modulus E_0. The insensitivity of k to the use of these 3 quantities arises from their linear relationship, as specified in the definition of the apparent density (Eq. 1). Moreover, others have reported that this exponential parameter does not have significant inter-site variability despite the significant variation found for the modulus-density relationships taken as a whole.[34] Furthermore, some authors have explicitly pooled results for the scaling parameter from various species and anatomical sites. For example, Gibson and Ashby concluded that the scaling parameter fell between 1 and 3 based on reviewing several previous studies using both human and bovine bone from various sites on the tibia and femur.[2] Carter and Hayes tested both cortical and trabecular specimens, of both human and bovine origin, and reported the modulus to vary as a cubic function of apparent density.[34] Goulet et al. reported an exponential factor range of 2 to 3, relating modulus to BVF for human samples taken from various anatomical sites.[35]

The parameter E_0 = 2562 MPa represents the modulus of the bone phase (BVF = 100%). The modulus of mature trabecular bone tissue (BVF = 100%) has been directly measured and reported by other groups. Experimental results using nano-indentation, as recently reviewed,[36] have ranged from E_0 = 8.02 ± 1.31 GPa for adult human vertebrae[30] to 21.5 ± 2.1 GPa for the porcine femur.[31] Moreover, Gibson and Ashby[2] reported a species-independent tissue modulus for trabecular bone of 12 GPa based upon review of the pertinent literature at the time. The parameter fit for the tissue modulus in the present study, 2.6 GPa, was lower than the previous reports. The difference could be due to inter-species variation and even more likely to the effect of age. For example, the present study used immature crania and younger skull specimens. Immature skull bones, from both the porcine and human cases, have been shown to be significantly more compliant than their adult counterparts.[8]

The homogenized modulus of the adolescent minipig cranial specimens was predicted to range between 378 and 786 MPa. This is the through-thickness modulus of all layers combined in series, and the results are comparable to values reported elsewhere for the through-thickness modulus of infant human and porcine specimens. For example, the bending modulus of parietal bone from human skulls of less than 1 year of age was reported as 461.1 ± 63.8MPa.[9] Likewise, the bending modulus of porcine infant bone was found to be 614 ± 96.2 MPa.[8] On the other hand, it is unclear how these through-thickness results correlate with that of the adult human skull, because there is significant variability in the reported human

skull values. For example, the modulus of adult human cranial specimens loaded in compression was reported in earlier studies to be an order of magnitude higher: 2.4 ± 1.5 GPa[5] and 1.39 GPa.[37] However, more recently Boruah et al. reported a modulus range of 450 ± 135MPa.[13] The variability in these reports likely arises from the multilayer structure inherent to the mature human skull but only partly present in younger specimens.

4.3 Underlying Assumptions and Limitations of the Mechanical Material Model

Mechanical parameters in this study were fitted to experimental results from Subset A, which consisted of only 4 samples taken from one skull. More importantly, the predictive power of the models was not validated with an independent dataset. Therefore, the relevancy of the fitted parameters to generic young minipig skulls can only be demonstrated by future studies in which the model predictions are compared with the results of other skulls.

Mechanical material modeling divided the depth dimension of the compressively loaded specimens into layers acting in series. The model was motivated by the measured bone volume fractions, which had a clear, repeatable depth-dependence and a lack of any consistent transverse dependence. The layered approximations were further motivated by the in situ observation of 2-D banding within the DIC-measured strain distribution. An example of the bands in the DIC results was shown in Fig. 12. The model required at least 3 overarching assumptions:

- The strain at each depth was uniform in the transverse dimension.
- There was negligible normal-shear coupling during the compression experiment.
- The initial stress-strain response of the specimen to quasi-static compression could be approximated with an elastic modulus.

4.3.1 Strain across the Transverse Plane

For the strain to be uniform across the transverse dimension, at least 2 conditions would need to be true. First, the morphology needs to be approximately constant across the transverse plane. Secondly, the bone material itself (BVF = 100%) needs to be approximately homogeneous apart from structural arrangement. This latter issue of treating the bone material as homogeneous, and therefore modeling any mechanical anisotropy as arising only from structural arrangement of the material, has been explicitly discussed elsewhere.[38] The remaining condition, the low level of structural anisotropy across the transverse plane of the skull, has not been

well-established. On one hand, the bone volume fraction has been reported as constant across the transverse plane in the human skull. For example, McElhaney et al.[5] examined serial sections of human cranial bone with an optical microscope, analogous to the μCT image stack of the present study but at lower resolution. He concluded that the porosity distribution across the transverse plane could be approximated as homogeneous, especially in comparison with the porosity variation in the depth direction. The present study reached the same conclusion with μCT data on the order of microns. Appendix A showed that the variation in the depth dimension was generally greater than the variation in the transverse plane.

On the other hand, the angle of the dominant bone direction within the specimens had a noticeable amount of variation across the transverse plane. This transverse variation would undermine the approximation that the strain is constant across the plane if the mechanical response of the cranium was known to be highly dependent upon the orientation of the bone. However, the effect of bone orientation on the mechanical response of cranial bone, specifically, has not been answered conclusively. For example, the extent to which the bone segments within the skull were aligned in the dominant direction, measured in part by the degree of anisotropy, was relatively low compared with canonical load-bearing bones such as the femur. The low DA could indicate that the structure does not have a strongly dominant direction, and therefore the variation in bone orientation is irrelevant.

In the future, the approximation of the invariance of strain in the transverse direction could be obviated through the use of digital volume correlation (DVC). This method gathers strain data over the entire 3-D volume rather than only the 2-D face. Others have already demonstrated the use of DVC in trabecular bone.[39]

4.3.2 Shear-Normal Coupling

The stress state resulting from the mechanical loading was approximated as consisting only of normal compressive stress. For this approximation to be valid, one requirement would be that the specimen was perfectly machined to a parallelepiped with flat and parallel sides, a gross approximation at best. For example, the stress-strain response of some layers shown in Appendix C had initial artifacts, likely due in part to irregular specimen geometries.

Both the shear strain (ε_{xy}) and the normal strain (ε_{yy}) also exhibited artifacts in the initial portion of the test. These artifacts were especially visible in the large initial variations of the ratio of shear to normal strains ($\varepsilon_{xy}/\varepsilon_{yy}$), shown in the (c) subfigures of Appendix C. However, care was taken to only use portions of the response after this strain ratio had stabilized. Furthermore, the portions used for mechanical analysis had ratios of the shear to normal strains that were generally

lower than $\varepsilon_{xy}/\varepsilon_{yy} < 0.20$ (Appendix C). Finally, the shear strain did not generally increase as a function of time during the test, as shown in the (b) subfigures of Appendix C.

4.3.3 Linear Elasticity

The response of the specimens to small loads was approximated as elastic, and efforts were taken to investigate the applicability of this approximation. In Appendix B, individual specimens were shown to almost completely recover strains as large as 3.5% (calculated as an average over the surface). Furthermore, the apparent far-field stress-strain response was shown to be approximately repeatable for a specimen that was cyclically loaded with an intervening recovery period (Fig. 11).

Generally however, the layer-specific stress-strain responses were nonlinear (Appendix C), and elasticity remained a first-order approximation. The range of the response used for fitting a linear elastic modulus was maintained as constant as possible, and local strains on the order of a few percentage points were used to stay within the small-strain regime. Therefore, this modulus would not predict the response at higher strain values. For example, the higher strain values of some of the stress-strain responses shown in Appendix C resembled the brittle crushing failure of elastic-brittle foams.[2] This was especially evident for those layers nearest the skin that had very low BVF values. In future studies, the initial linear modulus models proposed in this study will be extended to the nonlinear regime of the response.

4.4 Conclusion

The cranial bone morphology of the adolescent Göttingen minipig was quantified using μCT imaging with a resolution on the order of a few microns. The volume fraction of the bone and its orientation within the skull were calculated from the imaging. The compressive mechanical response of cranial bone was also studied. In situ optical DIC methods were used to measure the 2-D strain distribution along the thickness. A functionally gradient response across the through-thickness direction was observed in the morphology and the mechanical properties of the cranial bone.

The adolescent minipig skulls had denser bone near the brain that gradually transitioned to more porous bone near the skin. This arrangement diverged from previously reported studies on large-breed pigs and humans. It is believed that this gradient is a result of developmental processes in the young minipig that would change significantly with age. On the other hand, the present study confirmed historical reports that the bone volume fraction shows more variation in the depth direction than across the transverse plane.

The bone phase was observed in the μCT measurements to be only slightly structurally anisotropic at the far-field length scale, similar to previous reports for human and large-breed pig skulls. A phenomenological relationship between localized bone volume fraction and modulus was developed using a small subset of specimens. The model assumed structural and mechanical isotropy. The results were applied to the larger group of specimens to predict the modulus-depth dependence. These moduli were homogenized to calculate a through-thickness modulus ranging from 378 to 786 MPa. The bone tissue modulus was inferred from the fitted parameters of the isotropic model to be 2.6 GPa. Further studies would be needed to either account for mechanical anisotropy or conclusively rule out its effects. These studies would be greatly aided by measures of bone architecture that can capture localized variation with greater clarity than the MIL analysis used in the present work.

5. References

1. The CDC, NIH, DoD, and VA Leadership Panel. Report to Congress on traumatic brain injury in the United States: understanding the public health problem among current and former military personnel. Centers for Disease Control and Prevention (CDC), the National Institutes of Health (NIH), the Department of Defense (DoD), and the Department of Veterans Affairs (VA); 2013.

2. Gibson LJ, Ashby MF. Cellular solids: structure and properties. Cambridge (UK): Cambridge University Press; 1997.

3. Mow VC, Huiskes R. Basic orthopaedic biomechanics and mechano-biology. Third ed. Baltimore (MD): Lippincott Williams & Wilkins; 2005.

4. Dempster WT. Correlation of types of cortical grain structure with architectural features of the human skull. American Journal of Anatomy. 1967;120(1):7–31.

5. McElhaney JH, Fogle JL, Melvin JW, Haynes RR, Roberts VL, Alem NM. Mechanical properties of cranial bone. Journal of Biomechanics. 1970;3(5):495–511.

6. Sanborn B, Gunnarsson CA, Foster M, Moy P, Weerasooriya, T. Effect of loading rate and orientation on the compressive response of human cortical bone. Aberdeen Proving Ground (MD): Army Research Laboratory (US); 2015 May. Report No.: ARL-TR-6907.

7. Baumer TG, Powell BJ, Fenton TW, Haut RC. Age dependent mechanical properties of the infant porcine parietal bone and a correlation to the human. Journal of Biomechanical Engineering. 2009;131(11):111006.

8. Margulies SS, Thibault KL. Infant skull and suture properties: measurements and implications for mechanisms of pediatric brain injury. Journal of Biomechanical Engineering. 2000;122(4):364–371.

9. Coats B, Margulies SS. Material properties of human infant skull and suture at high rates. Journal of Neurotrauma. 2006;23(8):1222–1232.

10. Motherway JA, Verschueren P, Van der Perre G, Vander Sloten J, Gilchrist MD. The mechanical properties of cranial bone: the effect of loading rate and cranial sampling position. Journal of Biomechanics. 2009;42(13):2129–2135.

11. Rahmoun J, Auperrin A, Delille R, Naceur H, Drazetic P. Characterization and micromechanical modeling of the human cranial bone elastic properties. Mechanics Research Communications. 2014;60:7–14.

12. Hubbard RP. Flexure of layered cranial bone. Journal of Biomechanics. 1971;4(4):251–263.

13. Boruah S, Henderson K, Subit D, Salzar R, Shender B, Paskoff G. Response of human skull bone to dynamic compressive loading. Proceedings of the International Research Council on Biomechanics of Injury (IRCOBI) Conference; 2013 Sep 11–13; Gothenburg, Sweden. Vol. 13; p. 497.

14. Peterson J, Dechow PC. Material properties of the human cranial vault and zygoma. The Anatomical Record Part A: Discoveries in Molecular, Cellular, and Evolutionary Biology. 2003;274(1):785–797.

15. Peterson J, Dechow PC. Material properties of the inner and outer cortical tables of the human parietal bone. The Anatomical Record. 2002;268(1):7–15.

16. Chung DH, Dechow PC. Elastic anisotropy and off-axis ultrasonic velocity distribution in human cortical bone. Journal of Anatomy. 2011;218(1):26–39.

17. McPherson GK, Kriewall TJ. The elastic modulus of a fetal cranial bone: a first step towards an understanding of the biomechanics of fetal head molding. Journal of Biomechanics. 1980;13(1):9–16.

18. Sauleau P, Lapouble E, Val-Laillet D, Malbert CH. The pig model in brain imaging and neurosurgery. Animal. 2009;3(08):1138–1151.

19. Jung M, Breusch S, Daecke W, Gotterbarm T. The effect of defect localization on spontaneous repair of osteochondral defects in a Göttingen minipig model: a retrospective analysis of the medial patellar groove versus the medial femoral condyle. Laboratory Animals. 2009;43(2):191–197.

20. Growth curve and growth data for the Göttingen minipig. Ellegaard Göttingen Minipigs. 2014;42:3.

21. DiLeonardi AM, Gunnarsson CA, Sanborn B, Weerasooriya T. Orientation dependent mechanical response and quantification of cranial bone of the Göttingen pig. Proceedings of the SEM 2015 Annual Conference & Exposition on Experimental & Applied Mechanics; 2015 June 8–11; Costa Mesa, CA.

22. Gunnarsson CA, DiLeonardi AM, Weerasooriya T. Quantitative microstructural analysis and anisotropic mechanical response of Göttingen pig cranial bone. Proceedings of the 2015 International Mechanical Engineering Congress & Exposition; 2015 Nov 13–19; Houston, Texas.

23. Otsu, N. A threshold selection method from gray-level histograms. Automatica. 1975;11(285-296):23–27.

24. Harrigan T, Mann R. Characterization of microstructural anisotropy in orthotropic materials using a second rank tensor. Journal of Materials Science. 1984;19(3):761–767.

25. Tassani S, Öhman C, Baleani M, Baruffaldi F, Viceconti M. Anisotropy and inhomogeneity of the trabecular structure can describe the mechanical strength of osteoarthritic cancellous bone. Journal of Biomechanics. 2010;43(6):1160–1166.

26. Harrigan TP, Jasty M, Mann RW, Harris WH. Limitations of the continuum assumption in cancellous bone. Journal of Biomechanics. 1988;21(4):269–275.

27. Doube, Ml, Kłosowski MM, Arganda-Carreras I, Cordelières FP, Dougherty RP, Jackson JS, Schmid B, Hutchinson JR, Shefelbine SJ. BoneJ: free and extensible bone image analysis in ImageJ. Bone 47. 2010;(6):1076–1079.

28. Prot M, Saletti D, Pattofatto S, Bousson V, Laporte S. Links between mechanical behavior of cancellous bone and its microstructural properties under dynamic loading. Journal of Biomechanics. 2015;48(3):498–503.

29. Ranslow AN et al. Microstructural analysis of porcine skull bone subjected to impact loading. Proceedings of the 2015 ASME International Mechanical Engineering Congress and Explosion; 2015 Nov 13–19; Houston, TX.

30. Hoffler CE, Moore KE, Kozloff K, Zysset PK, Brown MB, Goldstein SA. Heterogeneity of bone lamellar-level elastic moduli. Bone 26. 2000;(6):603–609.

31. Ko CC, Douglas WH, Cheng YS. Intrinsic mechanical competence of cortical and trabecular bone measured by nanoindentation and microindentation probes. Proceedings of the 1995 Bioengineering Conference; 1995 June 28–July 2; Beaver Creek (CO). Cited in: Oftadeh R, Perez-Viloria M, Villa-Camacho JC, Vazire A, Nazarian A. Biomechanics and mechanobiology of trabecular bone: a review. Journal of Biomechanical Engineering. 2015;137(1):010802.

32. Helgason B, Perilli E, Schileo E, Taddei F, Brynjólfsson S, Viceconti M. Mathematical relationships between bone density and mechanical properties: a literature review. Clinical Biomechanics. 2008;23(2):135–146.

33. Morgan EF, Bayraktar HH, Keaveny TM. Trabecular bone modulus density relationships depend on anatomic site. Journal of Biomechanics. 2003;36(7):897–904.

34. Carter DR, Hayes WC. The compressive behavior of bone as a two-phase porous structure. The Journal of Bone & Joint Surgery. 1977;59(7):954–962.

35. Goulet RW, Goldstein SA, Ciarelli MJ, Kuhn JL, Brown MB, Feldkamp LA. The relationship between the structural and orthogonal compressive properties of trabecular bone. Journal of Biomechanics. 1994;27(4):375–389.

36. Oftadeh R, Perez-Viloria M, Villa-Camacho JC, Vaziri A, Nazarian A. Biomechanics and mechanobiology of trabecular bone: a review. Journal of Biomechanical Engineering. 2015;137(1):010802.

37. Robbins D, Wood J. Determination of mechanical properties of the bones of the skull. Experimental Mechanics. 1969;9(5):236–240.

38. Cowin S. Remarks on the paper entitled fabric and elastic principal directions of cancellous bone are closely related. Journal of Biomechanics. 1997;30(11):1191–1192.

39. Hussein AI, Barbone PE, Morgan EF. Digital volume correlation for study of the mechanics of whole bones. Procedia IUTAM. 2012;4:116–125.

Appendix A. Three-Dimensional Morphology Variation

A.1 Overview

Individual specimens had a functionally gradient structure in the depth dimension (defined in Fig. A-1 as the *y* dimension). Trends in this dimension were significant and repeatable between individual specimens. For example, the bone volume fraction (BVF) decreased from the brain-most surface to the skin-most surface. On the other hand, variations in the 2 other dimensions (*x* and *z*) were small and not repeatable from specimen to specimen. These dimensions were also referred to as the transverse dimensions, as they were transverse to the depth dimension.

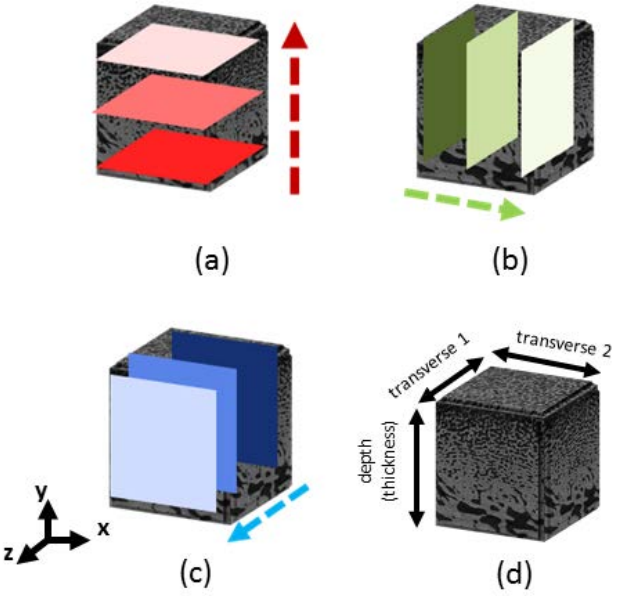

Fig. A-1 Schematics showing the relationship between the 3 image stacks: a) depth dimension (*y*), b) second transverse dimension (*x*), and c) first transverse dimension (*z*)

Different methods were used to examine the 3-D spatial variation of the morphology. In Section A.2, a case study is presented on Specimen 02-11, which was one of the specimens of Subset A used for mechanical-morphological analysis. Section A.3 examines the 3-D variation of BVF using digital cores extracted from the µCT dataset of each specimen in Subset A.

A.2 Case Study: Specimen 02-11

Specimen 02-11 was selected for a case study on intra-specimen morphology variation. Two methods were used. First, slice-by-slice averages of relevant parameters were calculated in all 3 dimensions. Then, the 3-D porous structure was visualized and the spatial distribution of the pore volumes was quantified. Both methods were based on the original µCT dataset of Specimen 02-11 (Section 2.2).

A.2.1 Slice-by-Slice Averages

Three μCT image stacks were created from the original dataset of 02-11. The first divided the depth dimension into an image stack with images in the *x*-*z* plane. This stack corresponded to the methodology described in Section 3.1.1 and used throughout the report. The other 2 stacks divided the 2 transverse dimensions into image stacks with images spanning either the *x*-*y* or *z*-*y* planes. The physical significance of the 3 image stacks is shown schematically in Fig. A.1.

The images of each stack were filtered (Gaussian, $\sigma = 2$) and binarized (Otsu 3D)[1] prior to quantitative analysis. The following parameters were calculated as an average over each image slice of the datasets: the BVF, trabecular thickness, and trabecular separation. The BVF parameter of the slice was previously presented in Section 3.1.1 of the main report as the ratio of the total bone area to the total area of the image. The trabecular thickness and separation were measures automatically calculated by the analysis software using the plate structural model (CTan, Bruker microCT).

Results are shown in Fig. A-2. The slice-by-slice averages are plotted as a function of the parameterized dimension in order to compare variation. The variation across the depth dimension is more profound than in the other dimensions and follows a clear trend. For example, the BVF drops by more than half in moving through the depth dimension while it only changes by roughly 10% in the other dimensions.

[1] Otsu N. A threshold selection method from gray-level histograms. Automatica. 1975;11(285–296):23–27.

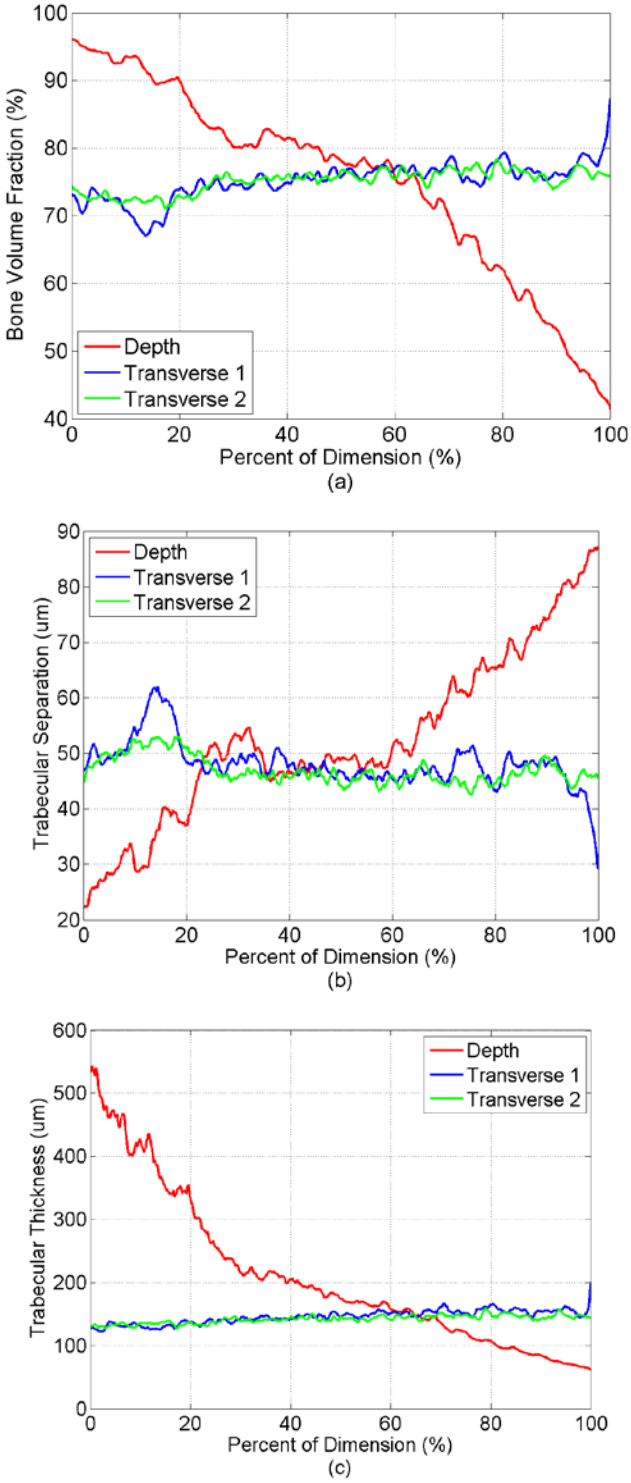

Fig. A-2 Variation of morphological parameters within Specimen 02-11

A.2.2 Three-Dimensional Pore Analysis

The µCT dataset of Specimen 02-11 was binarized such that white objects corresponded to pores rather than bone. The CTan software was then used to identify 3-D pore objects and find the position of each pore's centroid. Figure A-3 shows the 3-D pore objects. The position of each pore's centroid (*x*,*y*,*z* as in Fig. A-3) and its corresponding volume in cubic millimeters was determined. Figure A-4 shows the volume of each pore plotted as a function of the location of the pore's centroid along the thickness direction (a) and the 2 transverse directions (b and c).

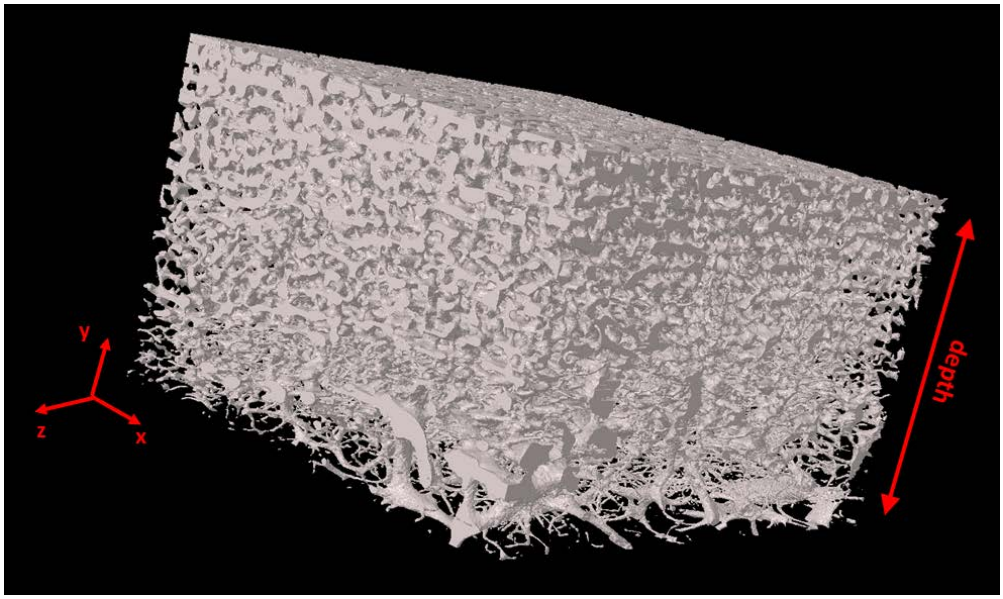

Fig. A-3 Volumetric rendering of the 3-D porous structure of Specimen 02-11

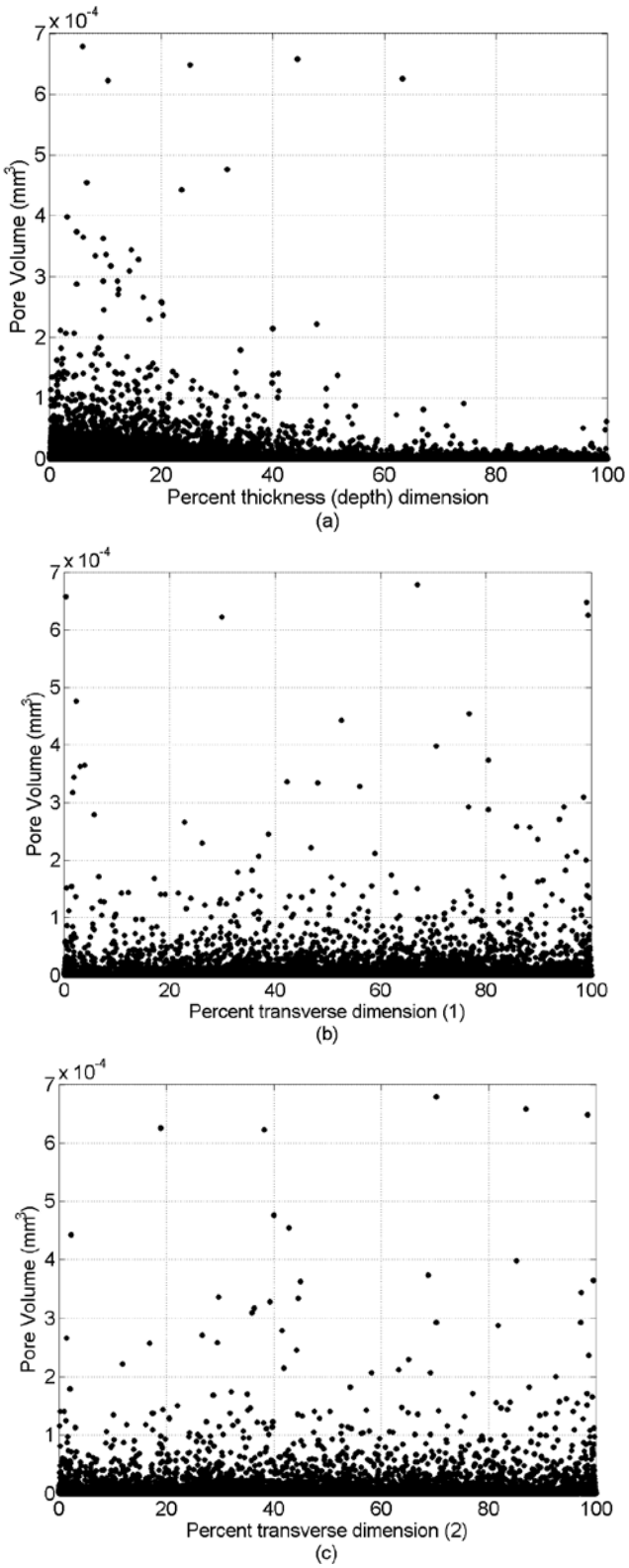

Fig. A-4 Volume of each pore plotted as a function of the pore centroid's depth dimension (a) and 2 transverse dimensions (b and c)

Each percentage point of the dimensions had a distribution of pore volumes that was heavily skewed to the right; there were many small pores but also many outliers with larger volumes. However, Fig. A-4 indicates that only the depth dimension shows any spatial trend in the pore volumes. In Fig. A-4a, the pore volume is seen to generally decrease with depth. The overall range of pore volumes also noticeably decreased as depth percentage increased. For example, between 0% and 20% depth, the pore volumes ranged from 0 to 7×10^{-4} mm^3, but from 80% to 100% depth the pore volumes only ranged from 0 to 0.5×10^{-4} mm. The other 2 dimensions (Figs. A-4b and A-4c) did not show these trends.

A.3 Three-Dimensional BVF Variation in the Sliding Volumes of Interest (VOIs)

The BVF analysis included in the body of the report, and in Section A.2.1, calculated BVF as an average over each image. However, each image consisted of the entire transverse plane (*x*-*z*). Therefore, only variation in the depth dimension (*y*) was studied by averaging over each image. To overcome this limitation, the digital cores which were created as part of the sliding VOI methodology were also used to quantify 3-D variation of BVF.

The sliding VOI method extracted digital cores from each specimen's μCT dataset, as described in Section 3.1.2 and Figs. 2c and 2d in the main report. Each core traversed the entire depth dimension (*y*) and was composed of square images in the transverse plane of side length *c*. Cores were separated from each other in the transverse plane. Therefore, the variation of BVF with depth, as measured within each core, could be compared with the variation of BVF across the transverse plane, as measured by the inter-core variation.

First, the image-by-image change of BVF was extracted from each core of the specimens in Subset A (Fig. A-5). The BVF was calculated as the average of each slice of the core. Slices were square images in the transverse plane (*x*-*z*) with side length *c*. The resulting image-by-image change of BVF was then averaged in the depth dimension (*y*) by the side length of the image: $y = c$. Figure A-6 shows the resulting depth-averaged BVF. The entire depth, *d*, was not generally divisible by the side length *c*. Therefore, the portions of the cores near the skin-most extreme (thickness percentages close to 100%) are shown in Fig. A-6 as averages over $y = mod(d,c)$, where *mod* refers to the modulo operation.

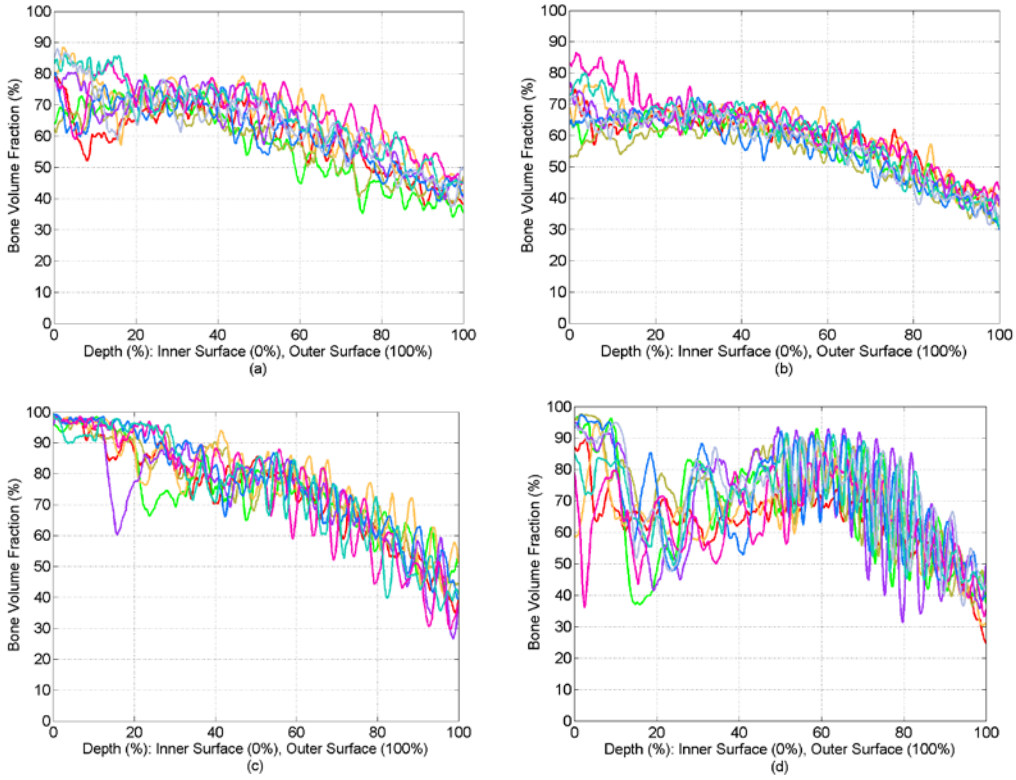

Fig. A-5 The BVF within each core of Subset A plotted as a function of thickness

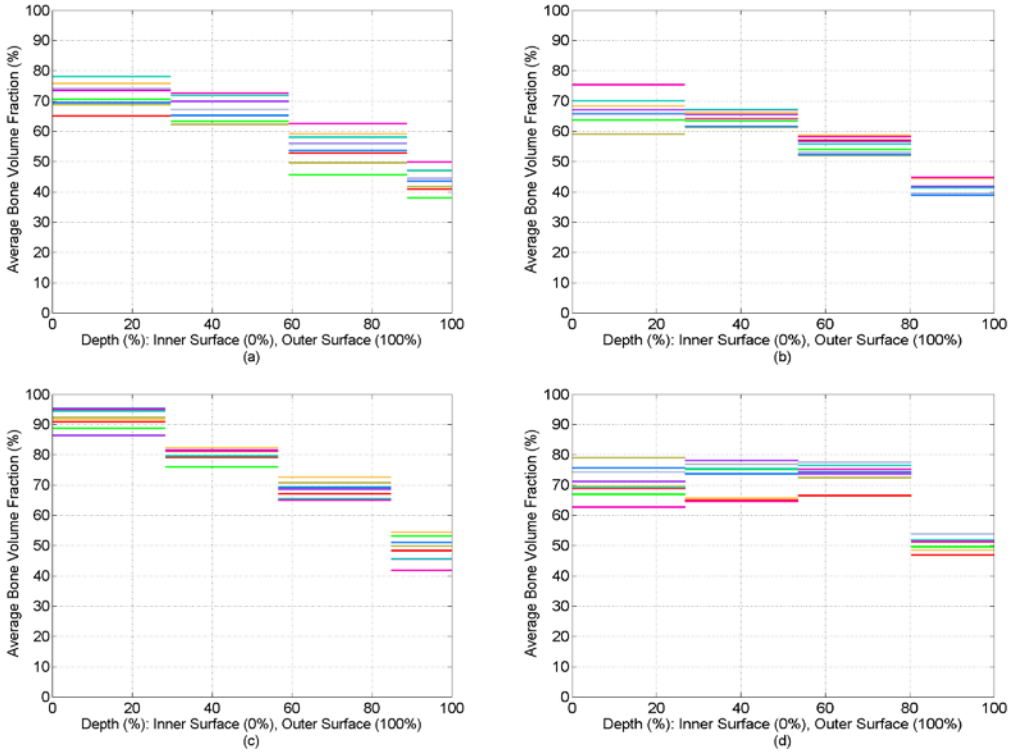

Fig. A-6 The BVF of each core (Fig. A-5), averaged in the thickness dimension by the side length of the image

Averaging in the depth dimension discretized the depth-dependent variation, which was shown in Fig. A-5, into "blocks". The blocks had a depth dimension equal to the transverse side length of the image slices (apart from those nearest to the outer surface). The variation of BVF across the transverse plane could then be visualized by the variation between the colors of a given block. Variation in the depth dimension was observed as the variation from block to block.

Specimen 02-11 (Fig. A-6c) showed the greatest amount of depth variation compared with transverse variation. In moving from 0% to 100% thickness, each of the 4 blocks had BVF values completely distinct from the other blocks. The variation across the transverse plane, shown as the variation between colors of each block, was always smaller than block-to-block (depth) variation.

The other specimens represented varying degrees of deviation from the ideal case of 02-11. For example, in Specimen 02-08 (Fig. A-6b), 3 of the 4 blocks were completely distinct. Specimen 02-15 (Fig. A-6d) had the most amount of transverse variation. The range of colors was greater than the block-to-block variation for the 3 blocks covering the thickness of 0%–80%. This indicated that the BVF variation across the transverse plane was on the same order, or greater, than the variation in the depth dimension for a depth up to 80%.

INTENTIONALLY LEFT BLANK.

Appendix B. Elastic Recovery of a Small Displacement Applied to Individual Specimens

B.1 Background

The mechanical analysis presented in Section 3.3 of the report treated the small-strain response of the specimens as linear elastic. Specifically, elastic moduli were fit to the localized stress-strain response for strains on the order of a few percentage points. The analysis implied that the individual specimens could elastically recover these small strains. The extent of this elastic recovery was further investigated by quantifying the recovery of a small applied displacement.

B.2 Method

Two specimens were used from Group A, both originating from Skull 03. These specimens were 03-04 and 03-05. The specimens were immersed in Hank's Balanced Salt Solution (HBSS) and compressed at a quasi-static rate in the depth dimension (*y*) as in Subset A (described in Section 2.3). The test included a single load/unload cycle followed by a substantial recovery period. Specimen 03-04 was tested to 10% apparent strain as calculated from far-field measurements and controlled using the crosshead displacement. After unloading, the specimen was left in the HBSS bath and allowed to recover for 130 h (about 5.5 days). Specimen 03-05 was tested to 5% apparent strain and allowed to recover for 130 min (about 2 h) in the HBSS bath.

One through-thickness face (*x-y)* of each specimen was speckled for digital image correlation (DIC) measurement as in Section 2.3. Images were captured of the speckled face both during the loading cycle and also throughout the recovery period.

B.3 Results

The strain in the loading direction, $\varepsilon_{yy}(x, y, t)$, was calculated for the *x-y* area of the speckled face at each time point by postprocessing the DIC data (Vic-2D 2009, Correlated Solutions Inc., Columbia, South Carolina). The strain was then averaged over the entire *x-y* area of the face. This measure of strain will be referred to as the area-averaged strain.

Figures B-1 and B-2 show the area-averaged strain during the tests of specimens 03-04 and 03-05, respectively. The area-averaged strain reached peak values far lower than the apparent strain that was calculated from the crosshead displacement. For example, Specimen 03-04 was loaded to an apparent strain of 10%, but the area-averaged strain only reached 3.83%. Specimen 03-05 was loaded to an apparent strain of 5%, but the area-averaged strain only reached 1.42%. These discrepancies are likely due in part to the large amount of strain gradient that occurred in the depth dimension during loading, as noted in the report (for example, Fig. 12). The overestimation of the apparent strain measures may also be due to machine compliance.

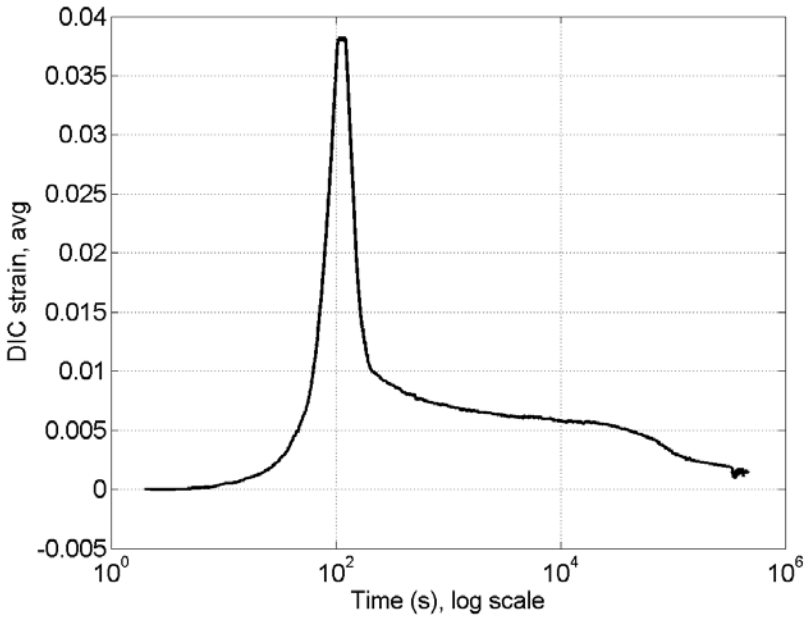

Fig. B-1 The area-averaged strain during the load-unload cycle and recovery of Specimen 03-04.

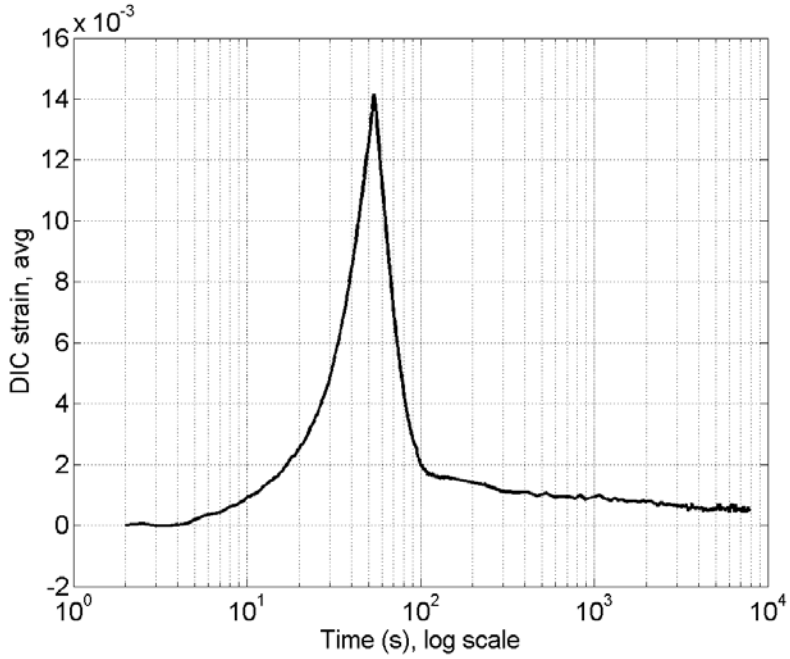

Fig. B-2 The area-averaged strain during the load-unload cycle and recovery of Specimen 03-05.

The percent recovery of each specimen was calculated from the difference between the peak strain reached during compression and the final strain at the end of the recovery period. Specimen 03-04 recovered 96.2% of the applied strain, and Specimen 03-05 recovered 96.4% of the applied strain.

The high recovery values indicated that a small amount of applied strain could be almost completely recovered when specimens are prevented from drying out due to hydration loss. A more detailed investigation in the future could attempt to find the localized strain response during recovery, similar to the localized strain response that was calculated in the body of the report. However, as a first approximation, the elastic limit appears to be at values of area-averaged strain that are greater than 3.5%.

Appendix C. Details Regarding the Elastic Modulus Fit of Each Layer's Stress-Strain Response

In Section 3.3, the specimens of Subset A were modeled by discretizing the depth dimension into 10 layers acting in series. The stress-strain response of each layer was then derived. An elastic modulus was found by fitting to the initial portion of the stress-strain response of 32 of the layers.

This appendix contains data relating to the fit of the elastic modulus. Data are presented as a figure for each of the 32 layers. Each figure (layer) has 4 subfigures. Subfigure (a) shows the stress-strain response of the layer. Subfigure (b) shows the normal strain in the direction of compression (ε_{yy}) and the shear strain (ε_{xy}) as a function of time during the test. Subfigure (c) includes the ratio of the shear strain and normal strains that were shown in subfigure (b): $\varepsilon_{xy}/\varepsilon_{yy}$. Subfigure (d) shows the number of DIC points that were extracted during each time point of the test.

The region of the stress-strain curve that was used to calculate the elastic modulus is shown in subfigure (a) in red coloring. The time domain that corresponded to this region is also indicated in the remaining subfigures (c and d) by red coloring. Moreover, in subfigure (c), the average value of the shear/normal strain ratio over the time domain of the fit is included in the figure legend. In subfigure (d) the average number of DIC points for each time point for the region of fit is also included in the figure legend.

Each layer will be referred to by its specimen of origin and also its corresponding depth percentage. As in the report, depth percentage ranged from 0% at the brain-most surface to 100% at the skin-most surface. The figure numbers for Figs. C-1 through C-32 are shown in Table C-1. Note that the brain-most layer, from 0% to 10% thickness, was not used for any of the specimens.

Table C-1 Figure numbers for each of the 32 layers

Spec. name	10–20 (%)	20–30 (%)	30–40 (%)	40–50 (%)	50–60 (%)	60–70 (%)	70–80 (%)	80–90 (%)	90–100 (%)
02-07	C.1	C.2	C.3	C.4	C.5	C.6	C.7	C.8	NU
02-08	C.9	C.10	C.11	C.12	C.13	C.14	C.15	C.16	C.17
02-11	NU	C.18	C.19	C.20	C.21	C.22	C.23	C.24	C.25
02-15	NU	NU	C.26	C.27	C.28	C.29	C.30	C.31	C.32

Note: NU = not used.

Specimen 02-07

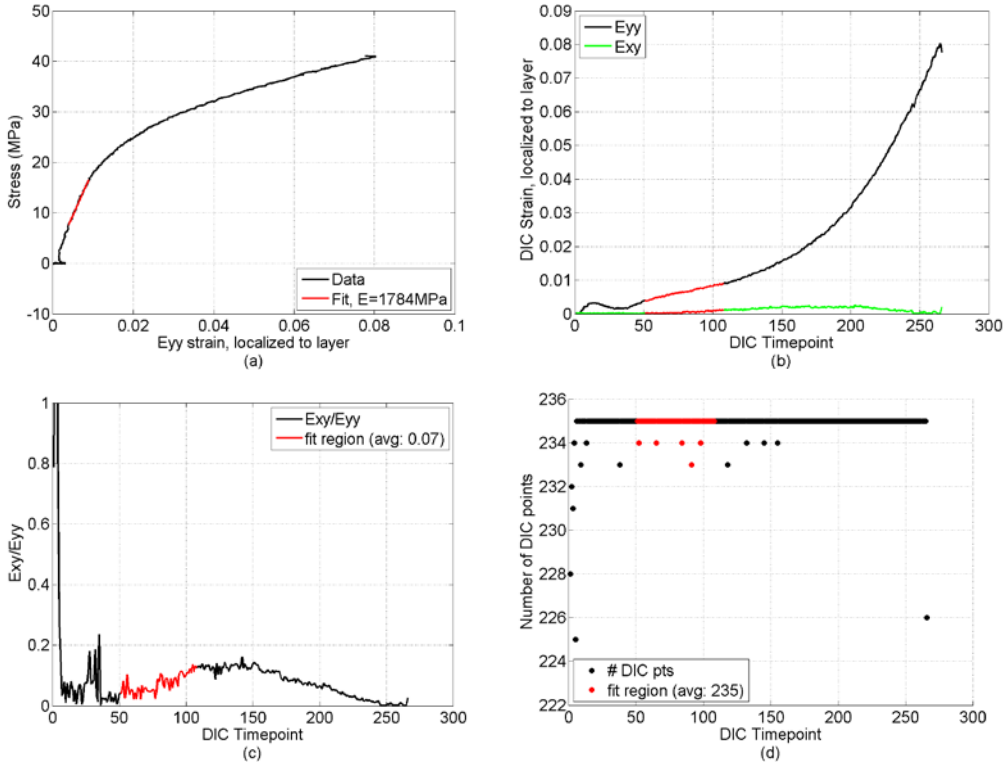

Fig. C-1 Specimen 02-07, layer from 10% to 20% depth

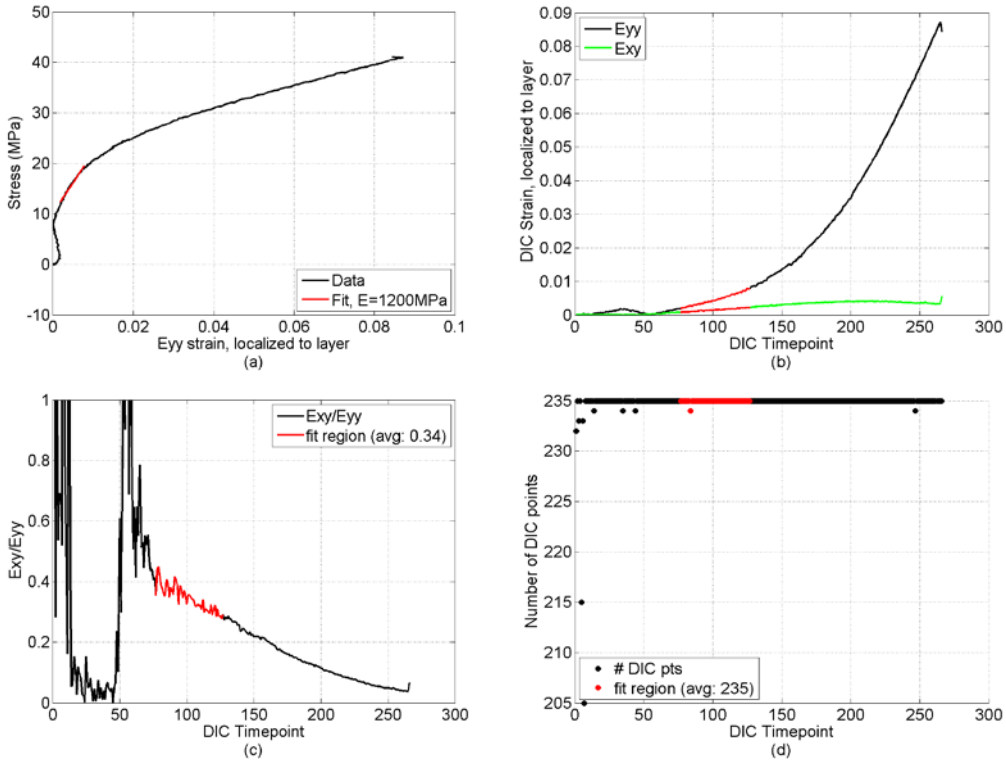

Fig. C-2 Specimen 02-07, layer from 20% to 30% depth

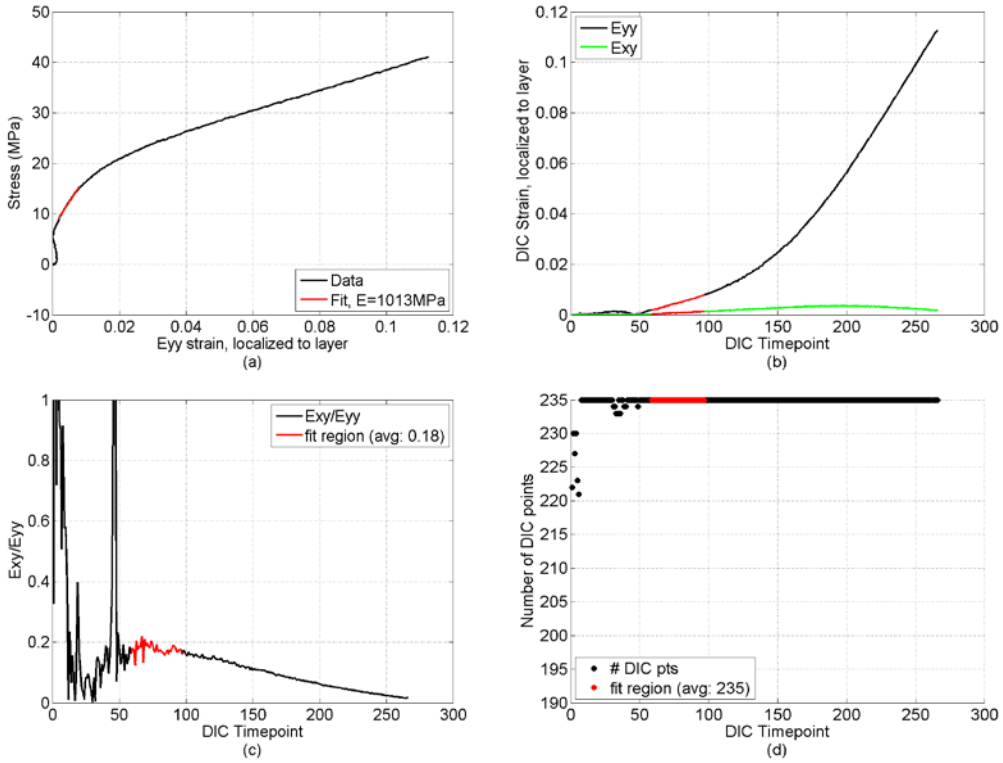

Fig. C-3 Specimen 02-07, layer from 30% to 40% depth

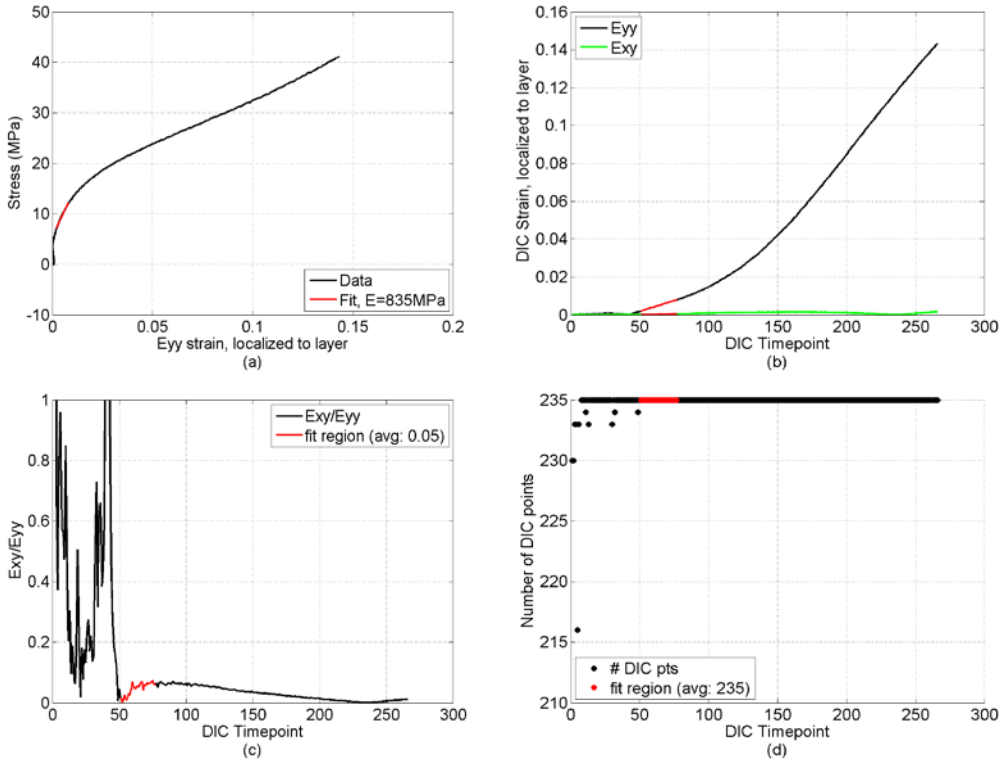

Fig. C-4 Specimen 02-07, layer from 40% to 50% depth

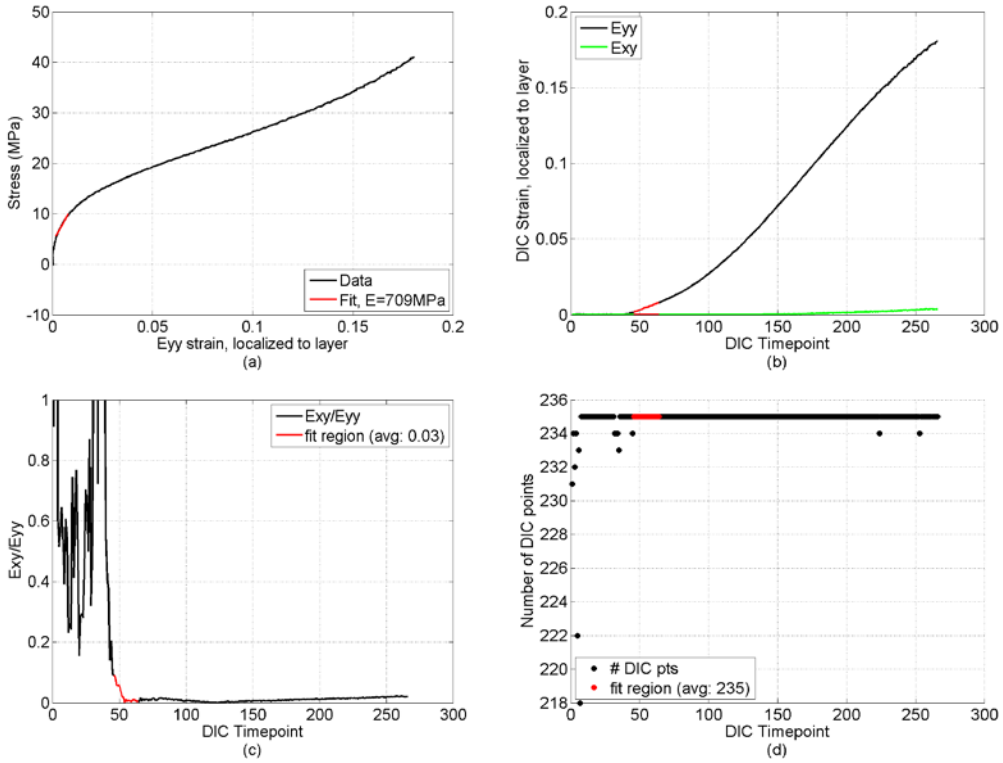

Fig. C-5 Specimen 02-07, layer from 50% to 60% depth

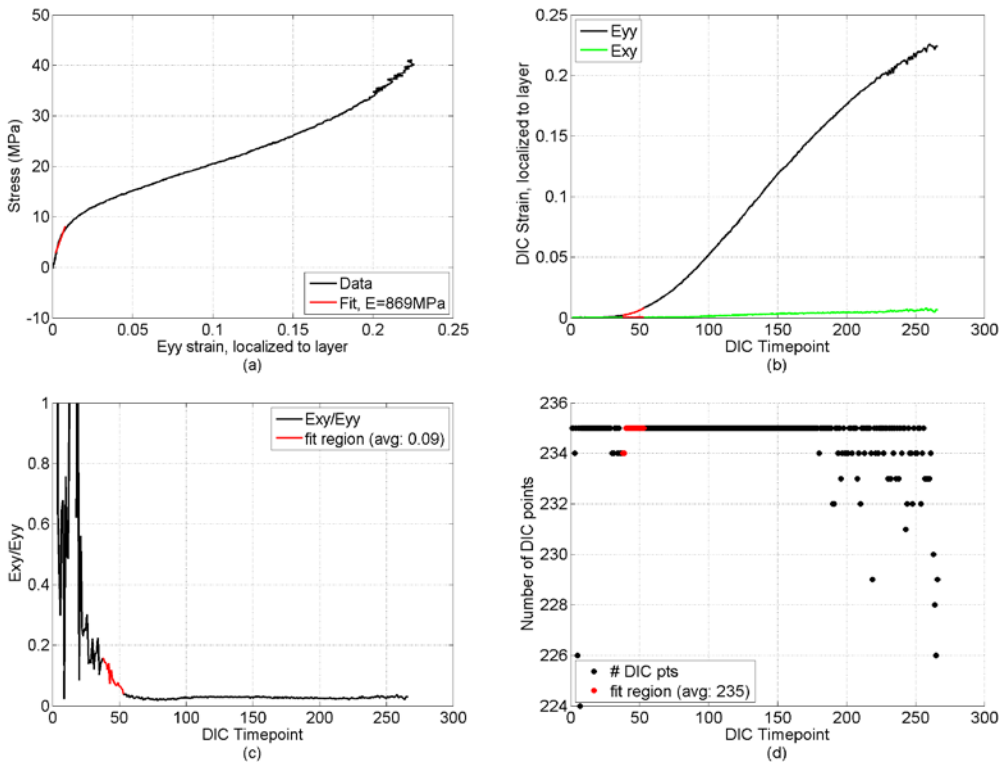

Fig. C-6 Specimen 02-07, layer from 60% to 70% depth

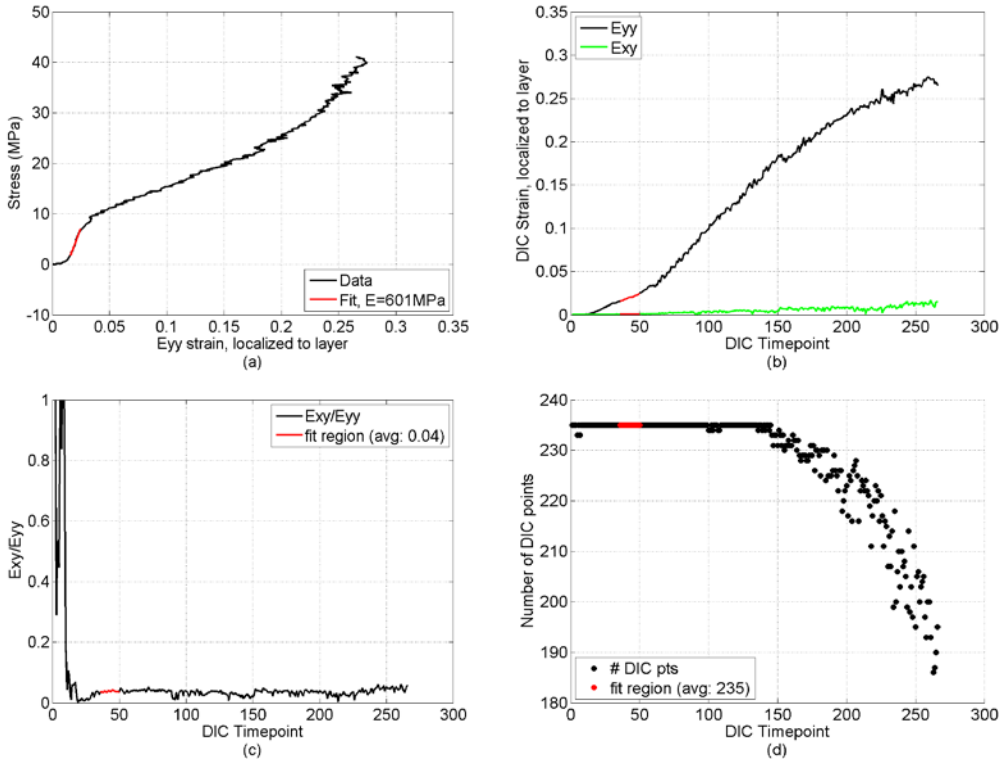

Fig. C-7 Specimen 02-07, layer from 70% to 80% depth

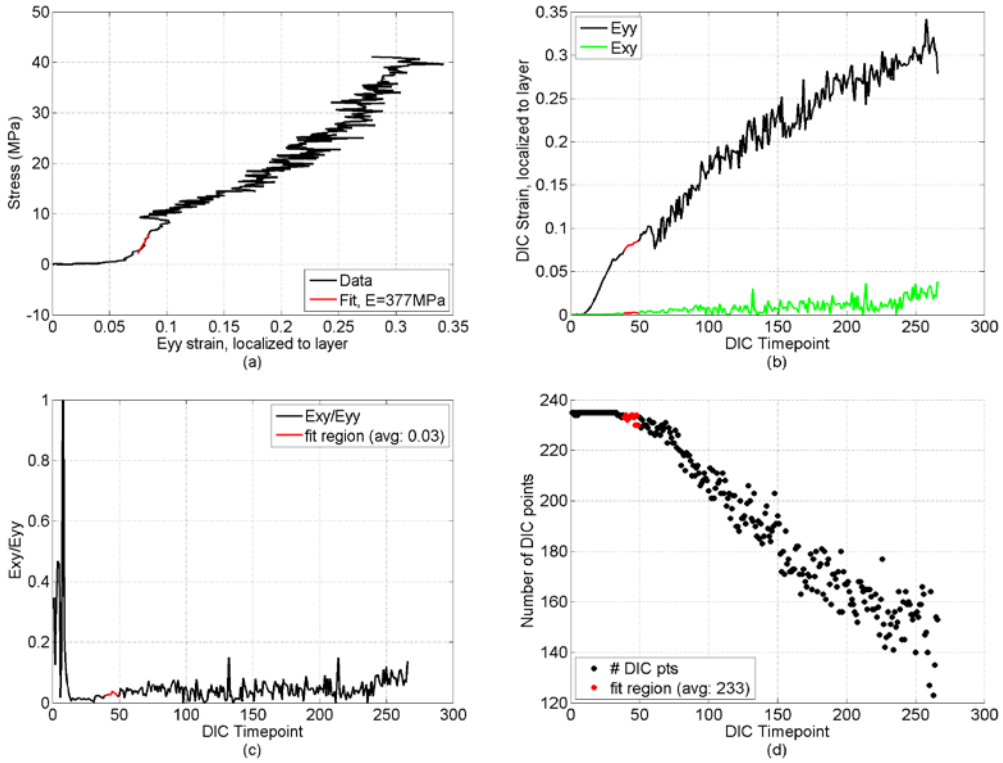

Fig. C-8 Specimen 02-07, layer from 80% to 90% depth

Specimen 02-08

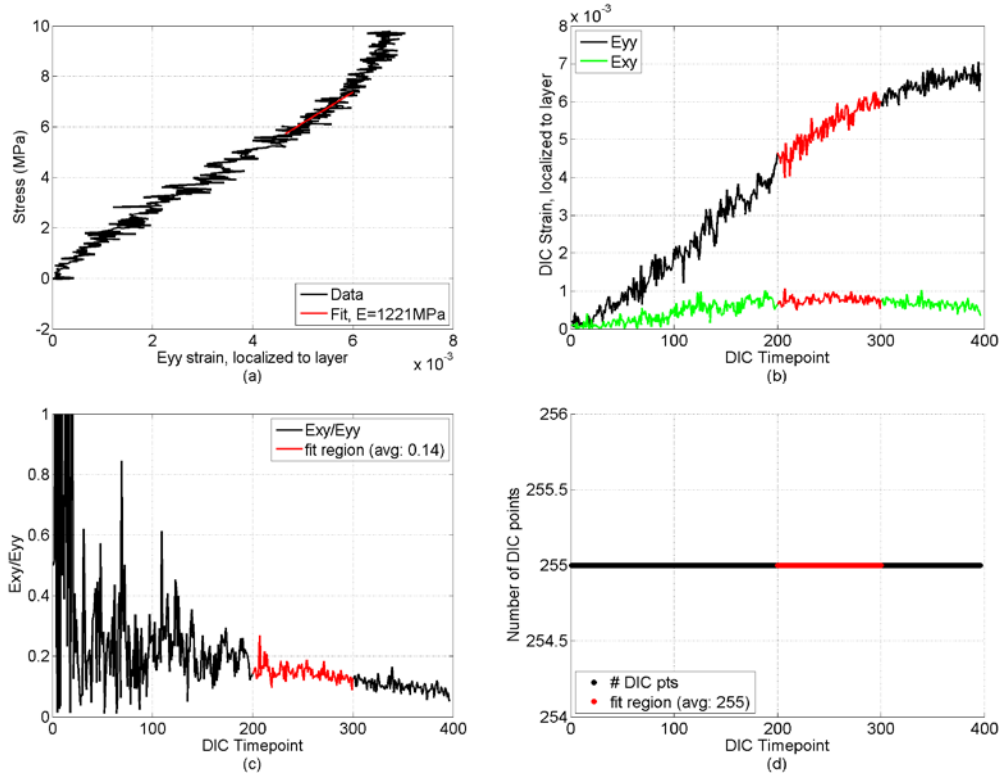

Fig. C-9 Specimen 02-08, layer from 10% to 20% depth

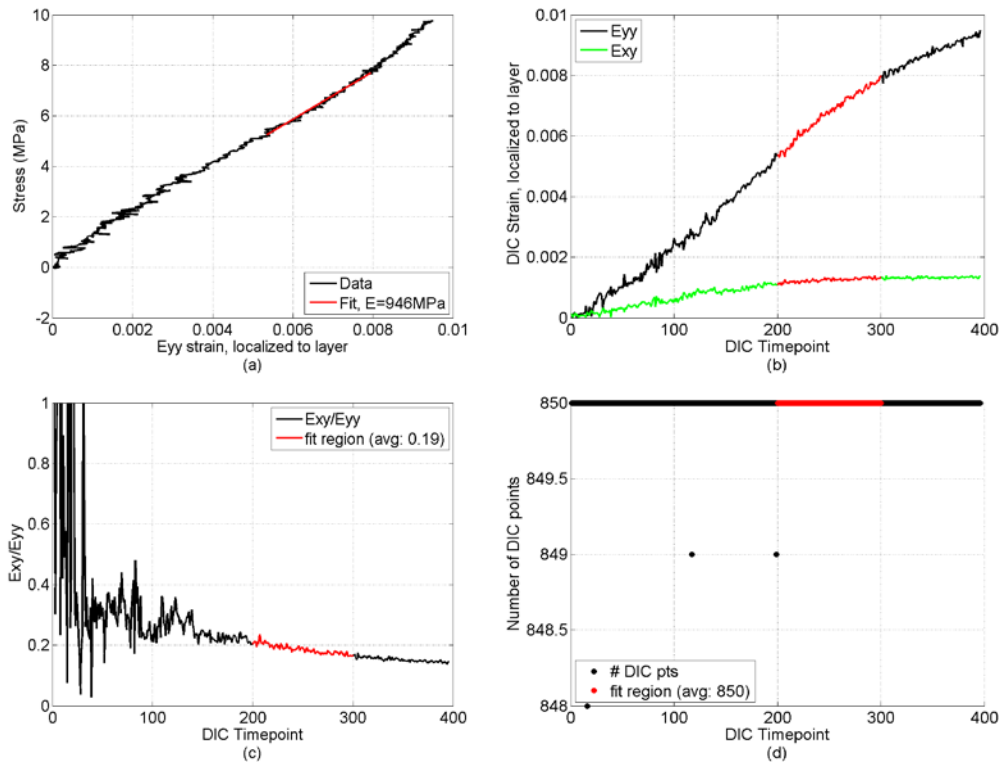

Fig. C-10 Specimen 02-08, layer from 20% to 30% depth

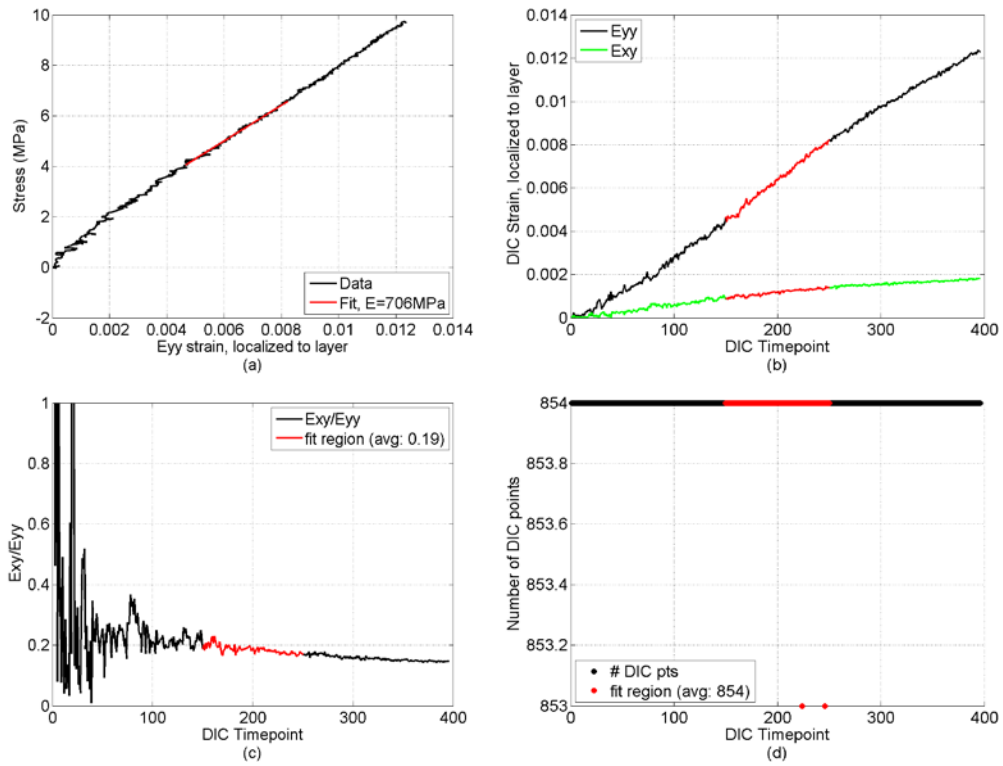

Fig. C-11 Specimen 02-08, layer from 30% to 40% depth.

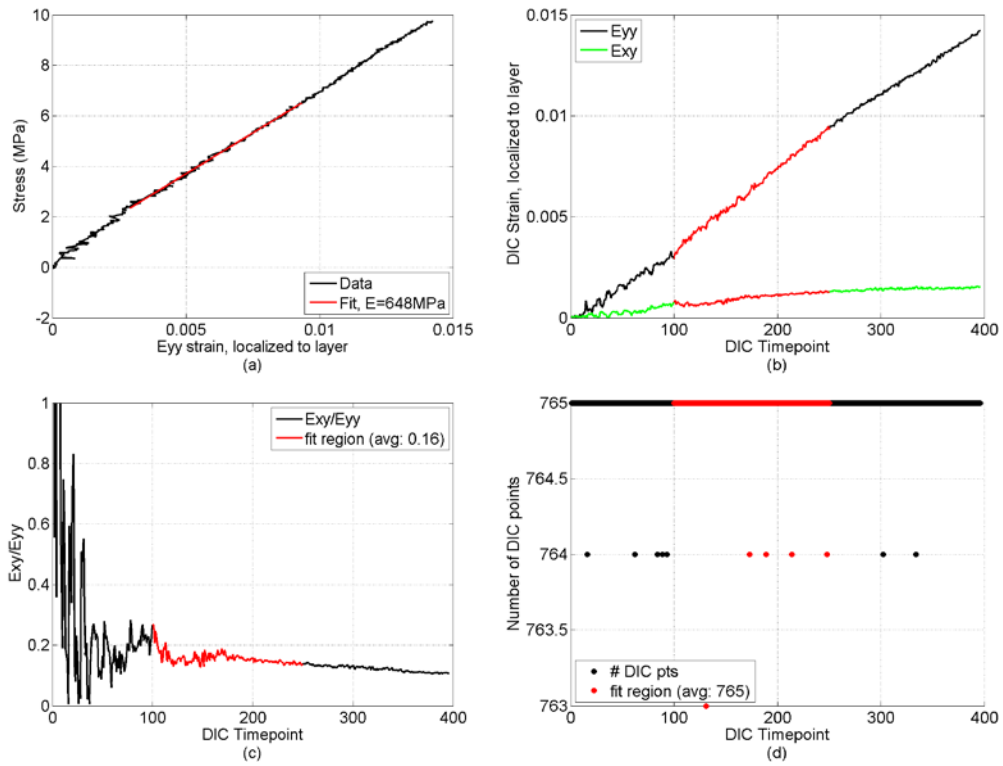

Fig. C-12 Specimen 02-08, layer from 40% to 50% depth

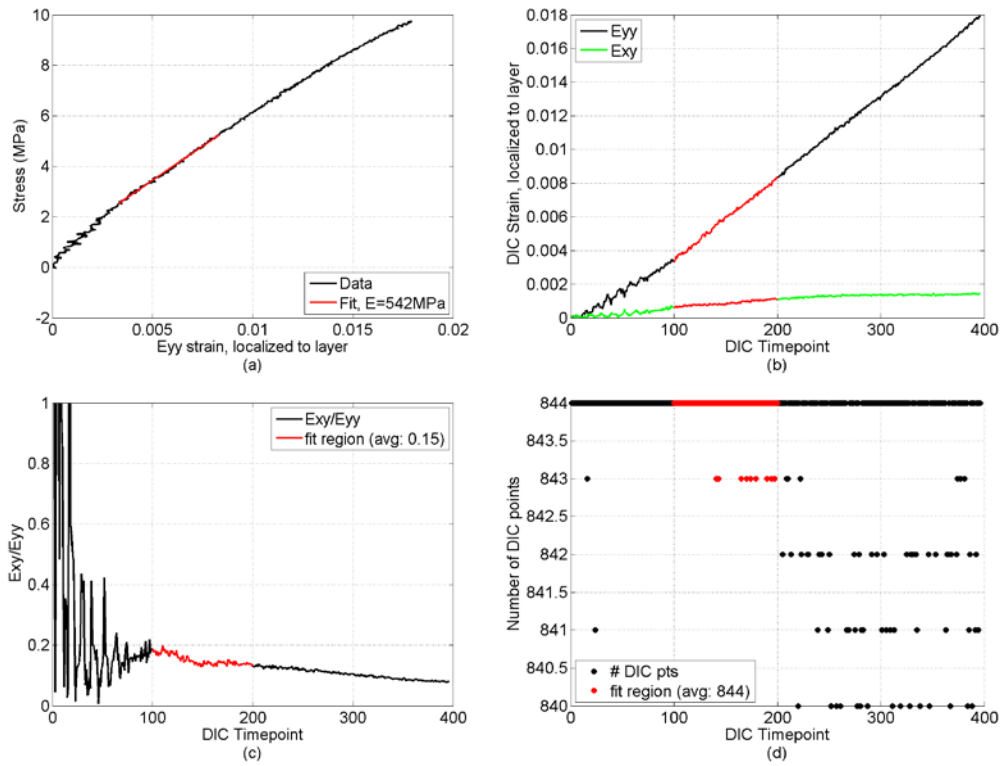

Fig. C-13 Specimen 02-08, layer from 50% to 60% depth

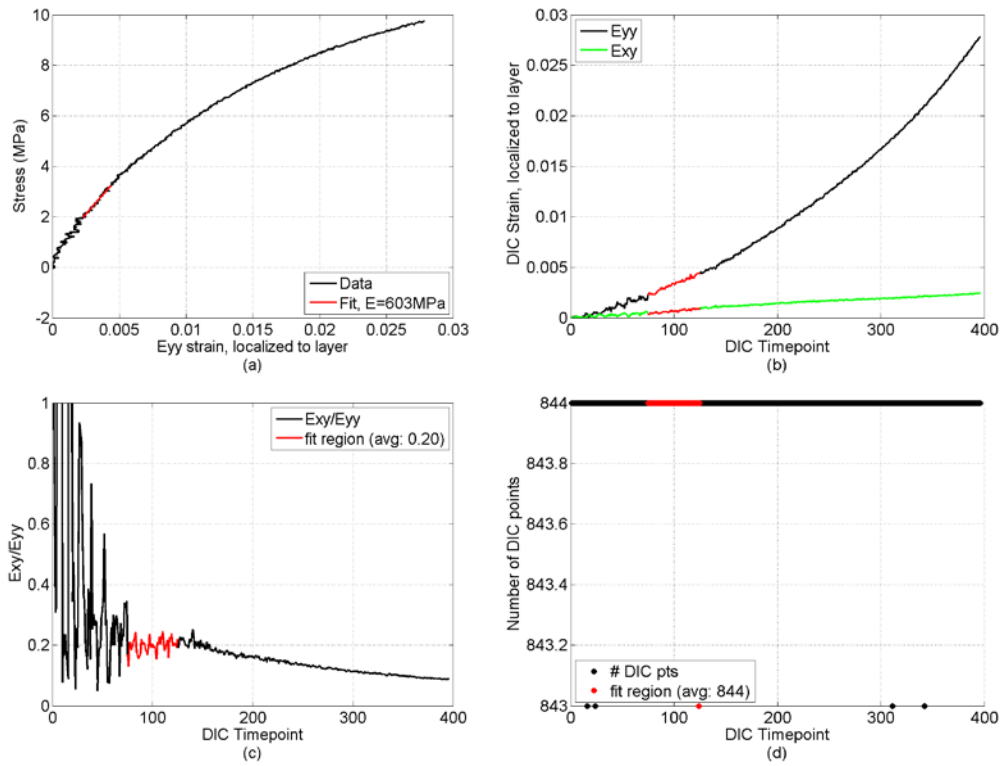

Fig. C-14 Specimen 02-08, layer from 60% to 70% depth

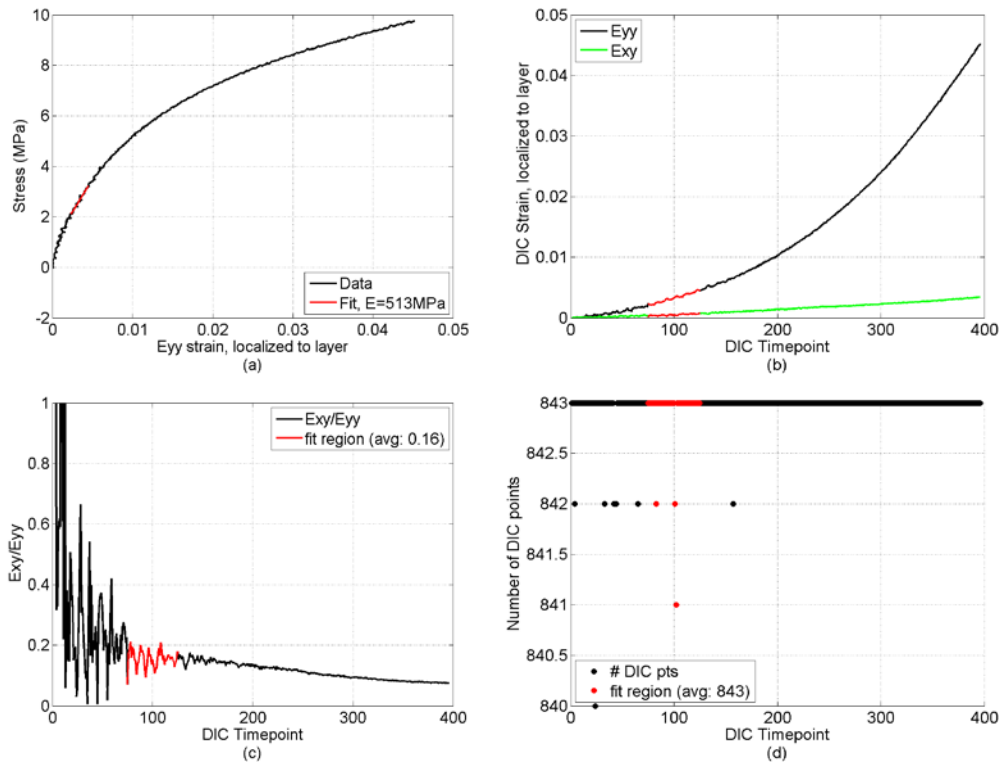

Fig. C-15 Specimen 02-08, layer from 70% to 80% depth

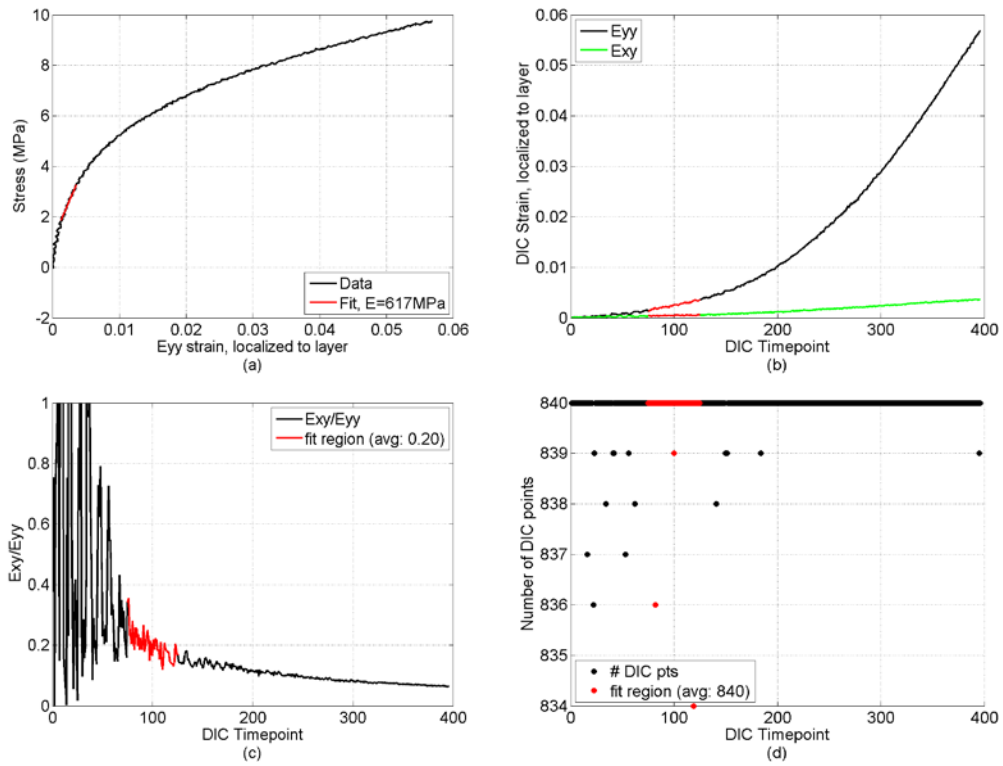

Fig. C-16 Specimen 02-08, layer from 80% to 90% depth

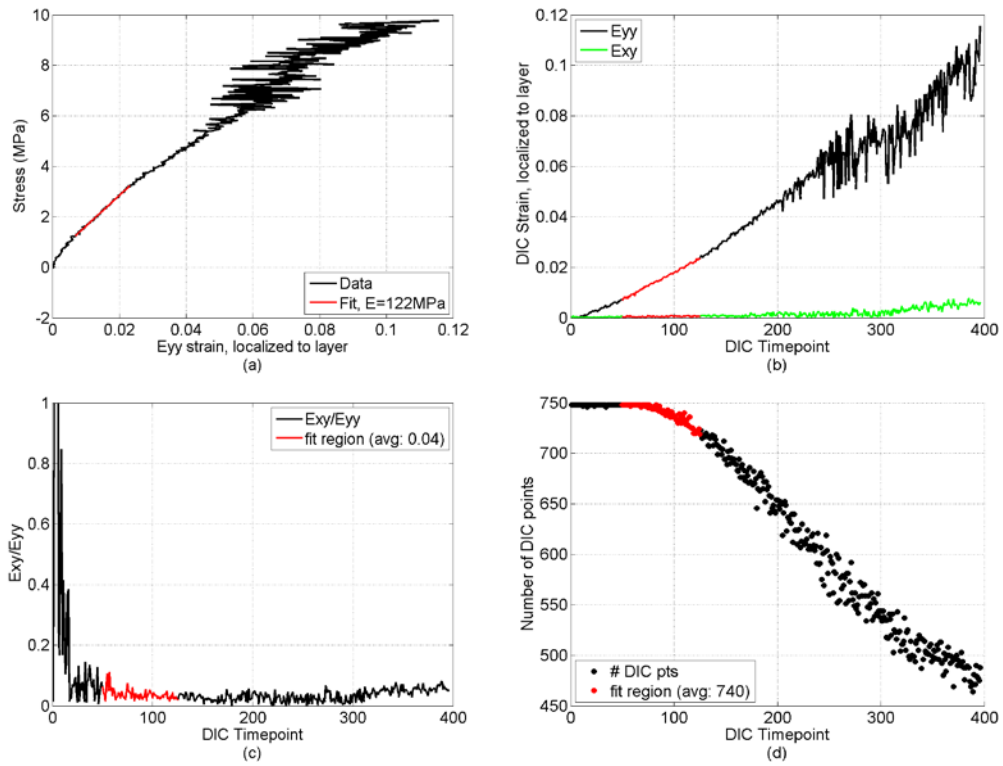

Fig. C-17 Specimen 02-08, layer from 90% to 100% depth

Specimen 02-11

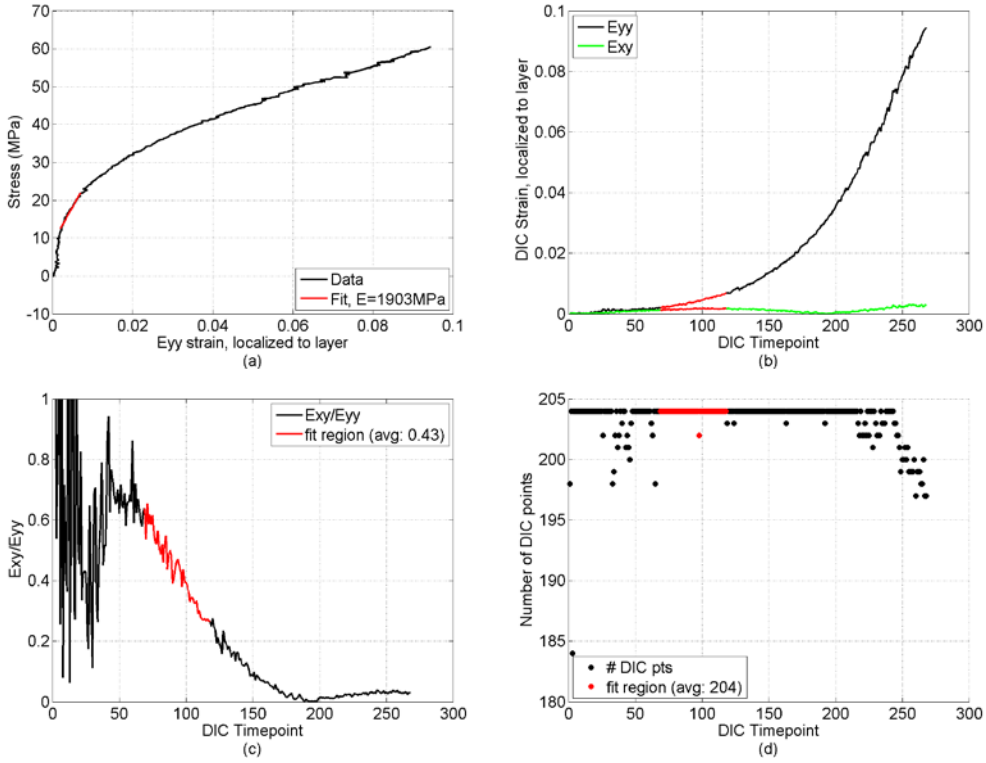

Fig. C-18 Specimen 02-11, layer from 20% to 30% depth

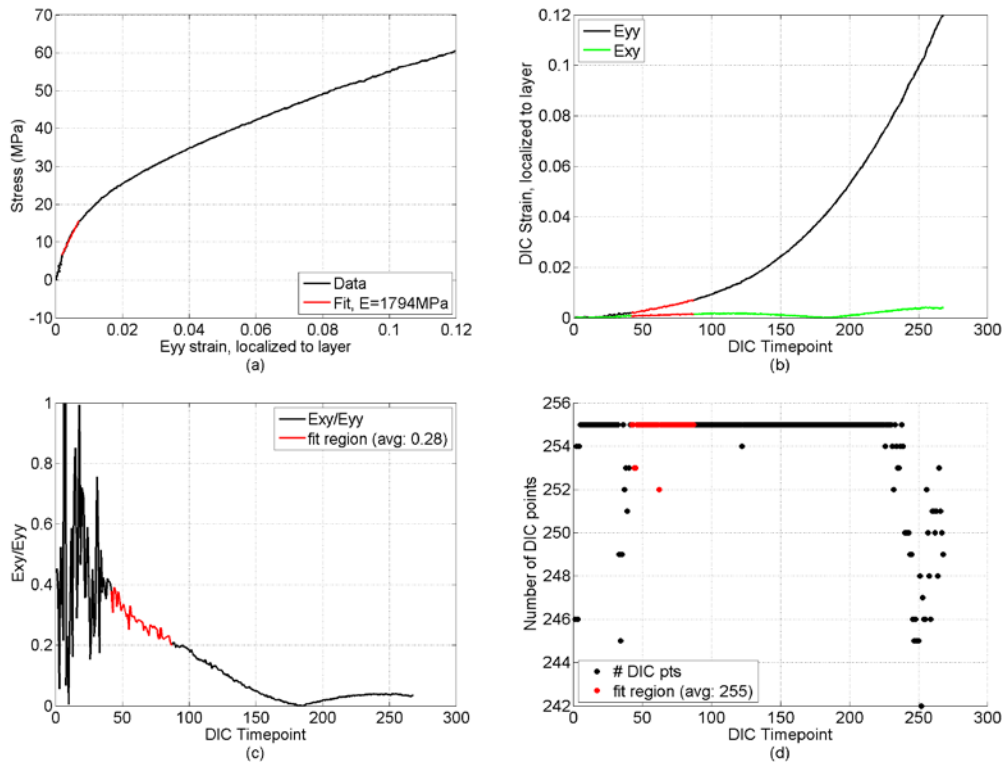

Fig. C-19 Specimen 02-11, layer from 30% to 40% depth

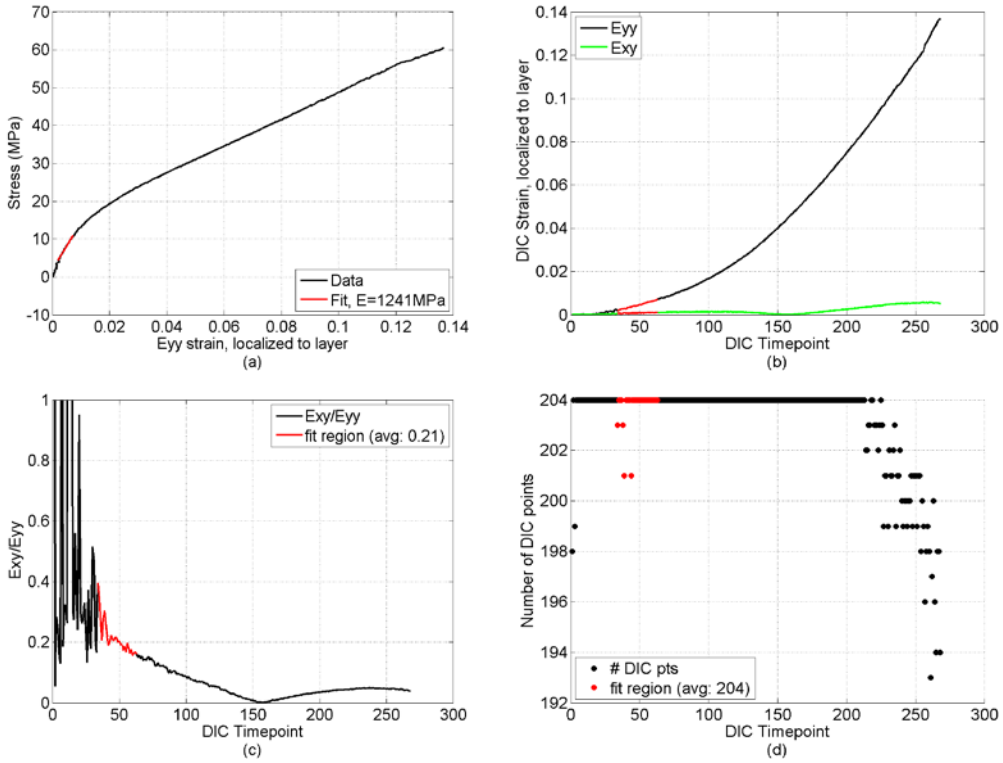

Fig. C-20 Specimen 02-11, layer from 40% to 50% depth

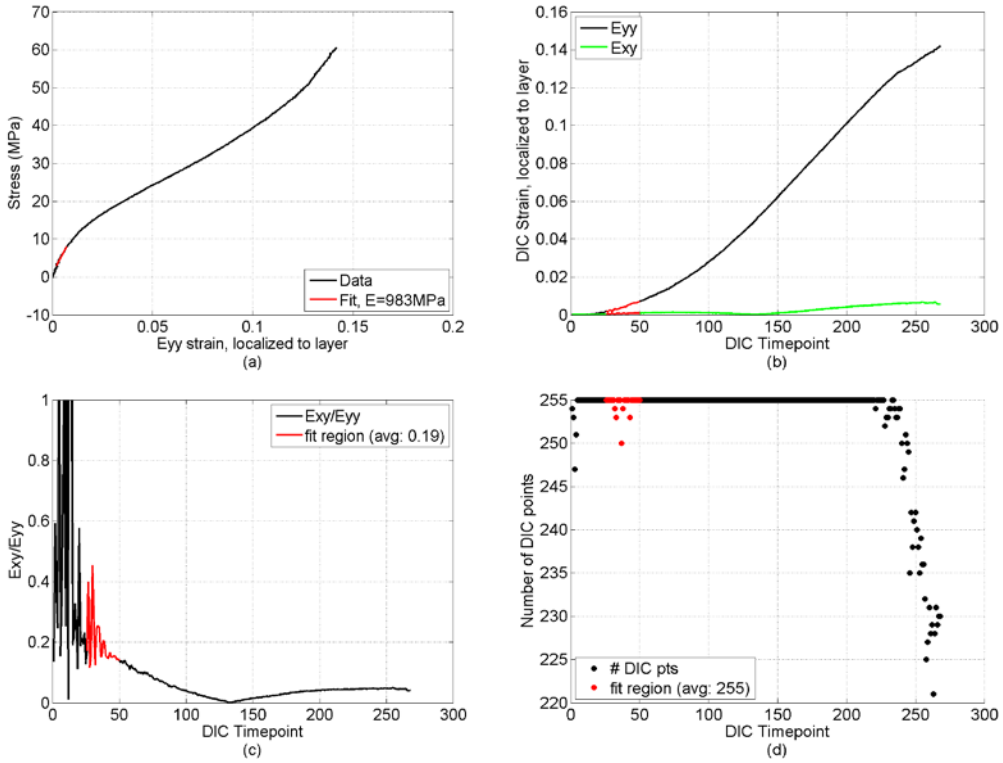

Fig. C-21 Specimen 02-11, layer from 50% to 60% depth

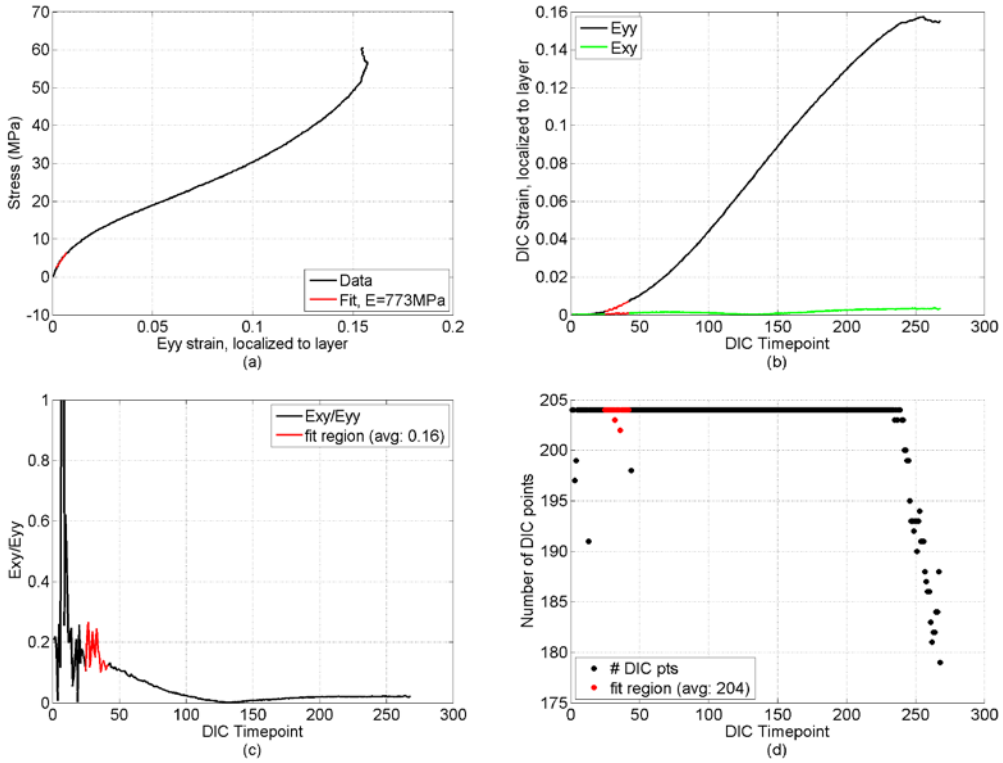

Fig. C 22 Specimen 02-11, layer from 60% to 70% depth

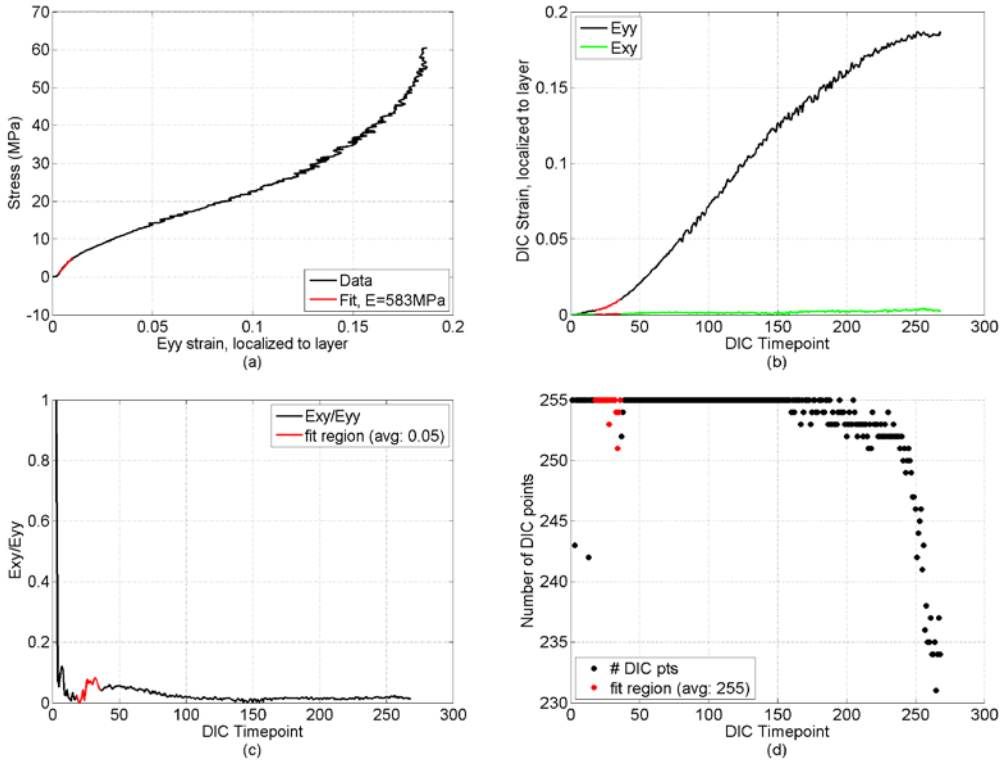

Fig. C-23 Specimen 02-11, layer from 70% to 80% depth

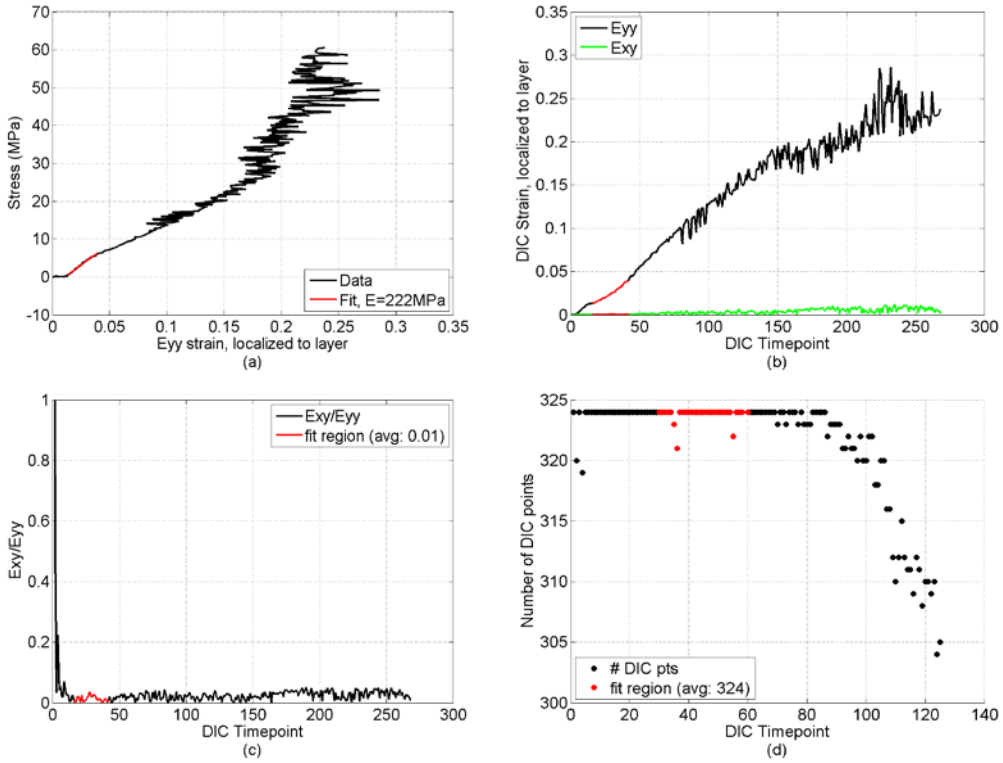

Fig. C-24 Specimen 02-11, layer from 80% to 90% depth

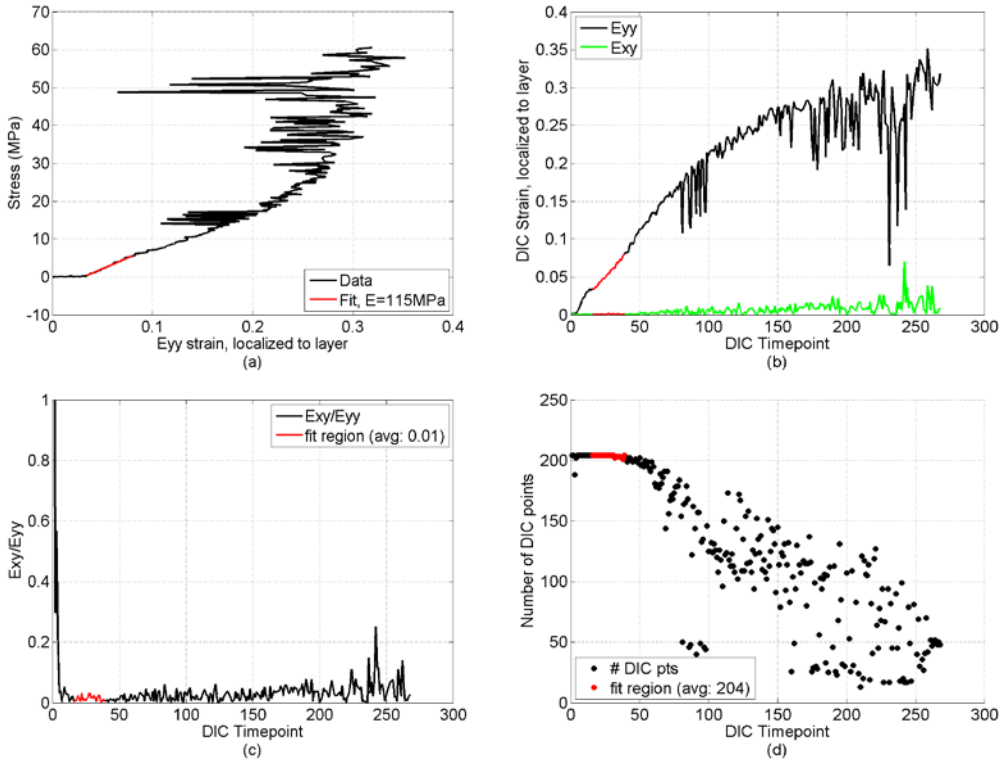

Fig. C-25 Specimen 02-11, layer from 90% to 100% depth

Specimen 02-15

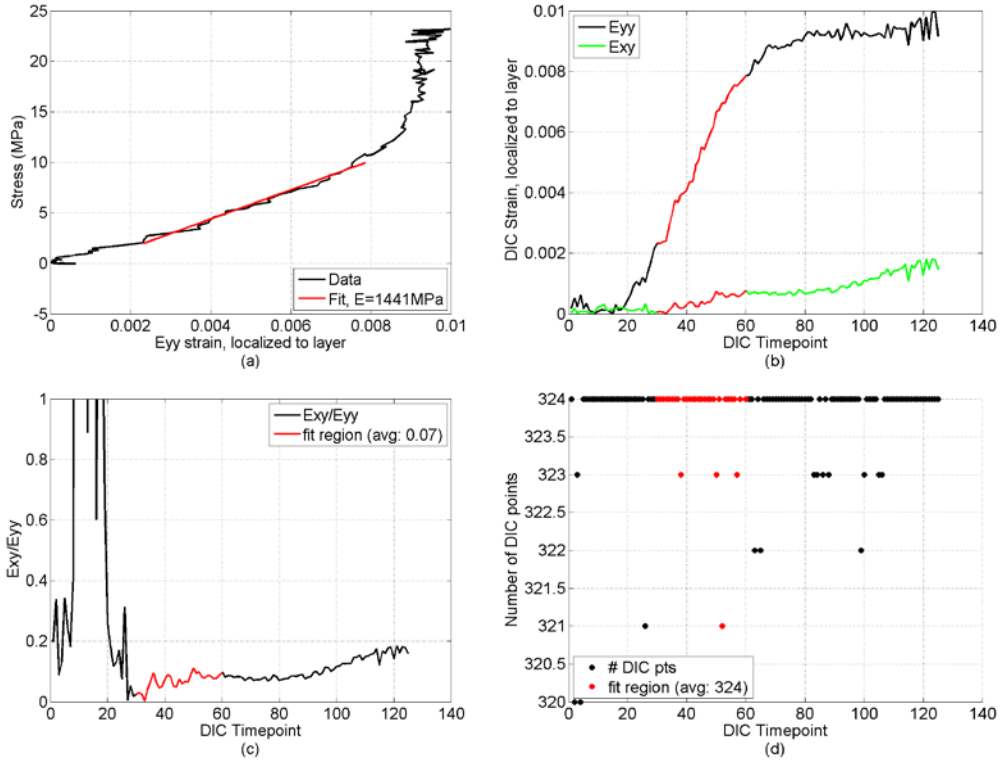

Fig. C-26 Specimen 02-15, layer from 30% to 40% depth

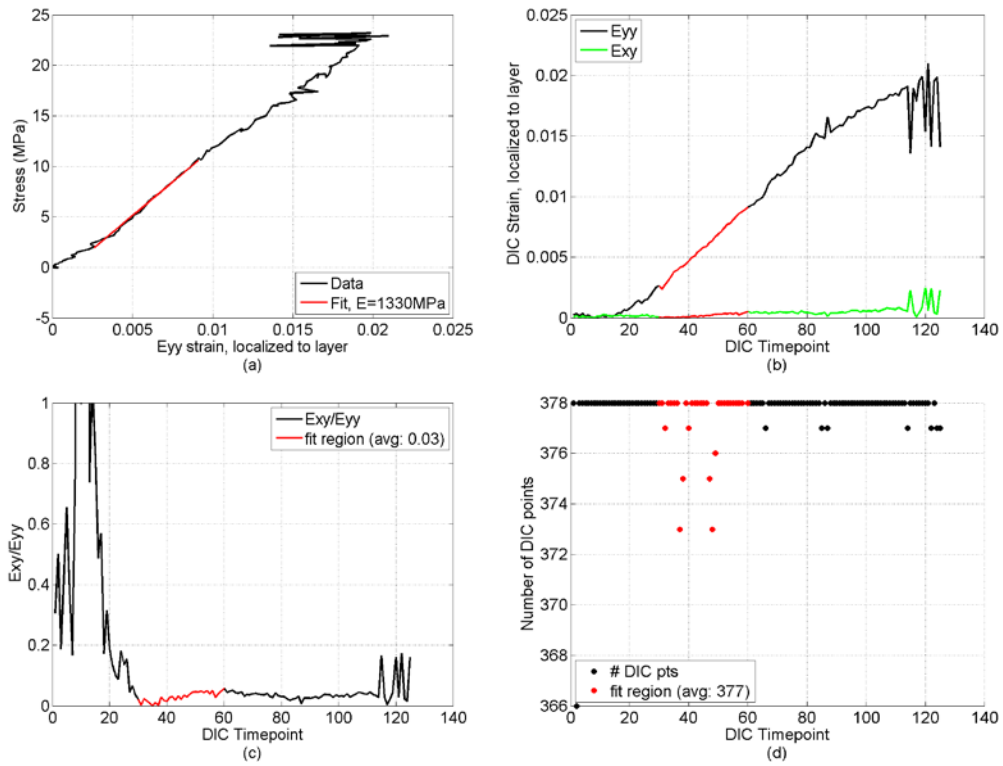

Fig. C-27 Specimen 02-15, layer from 40% to 50% depth

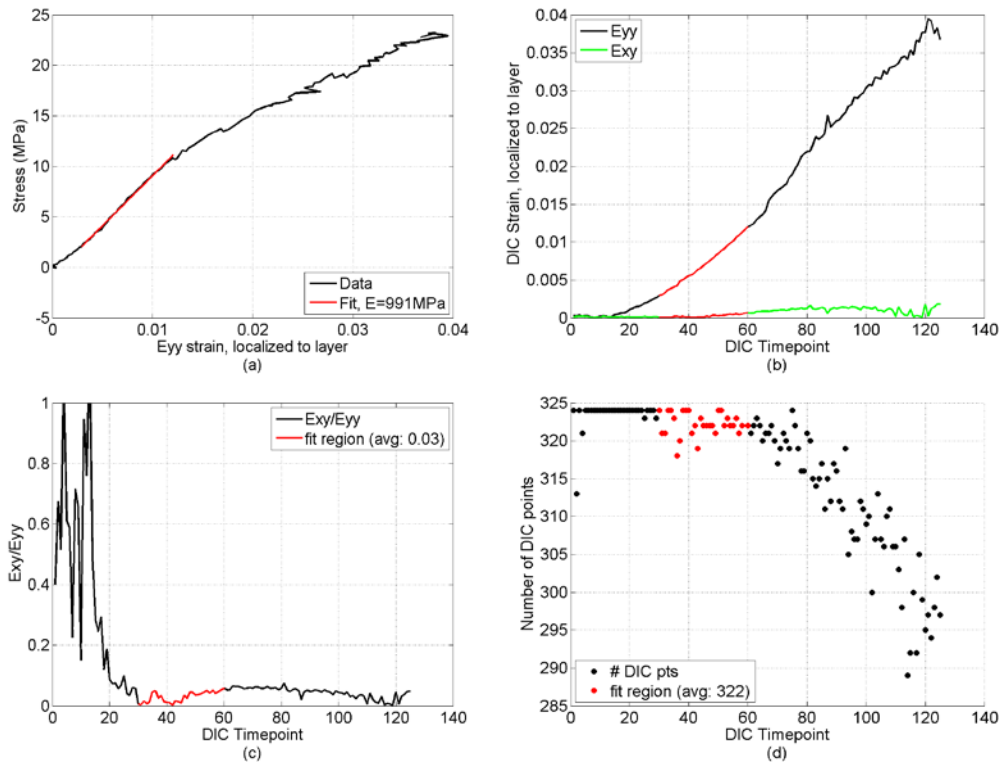

Fig. C-28 Specimen 02-15, layer from 50% to 60% depth

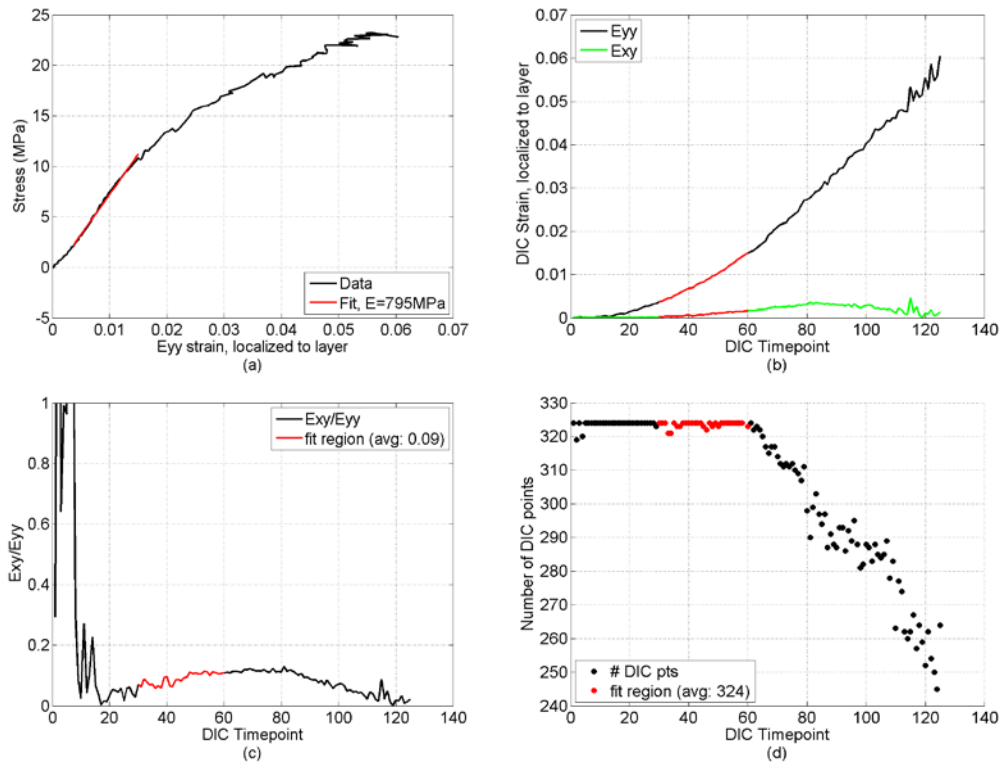

Fig. C-29 Specimen 02-15, layer from 60% to 70% depth

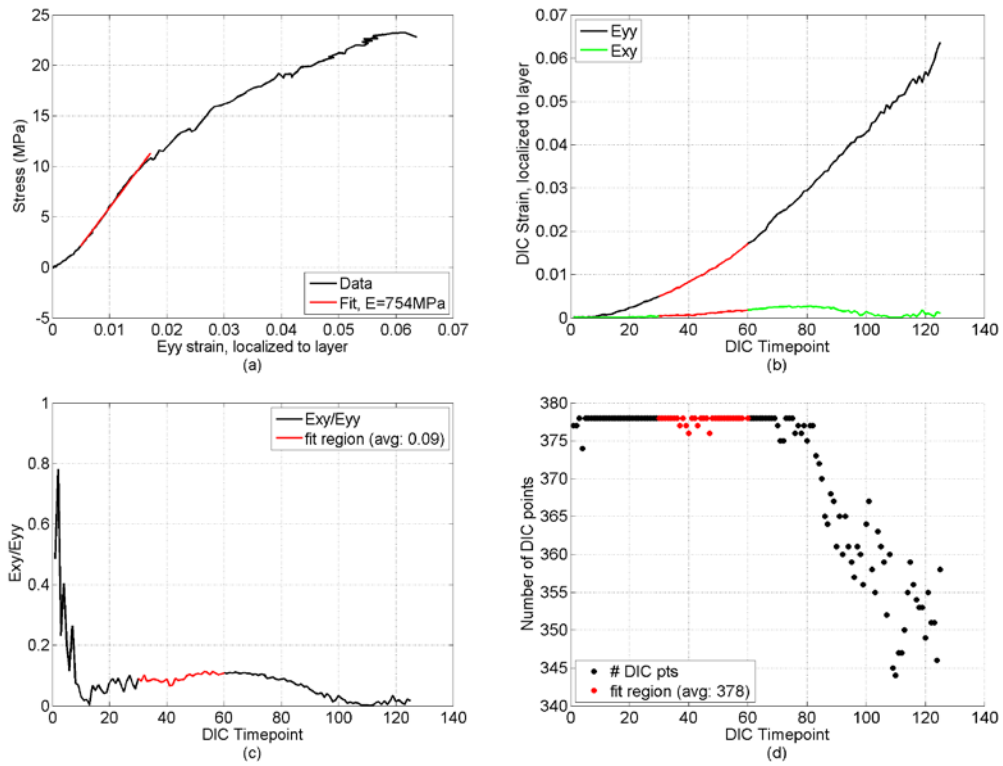

Fig. C-30 Specimen 02-15, layer from 70% to 80% depth

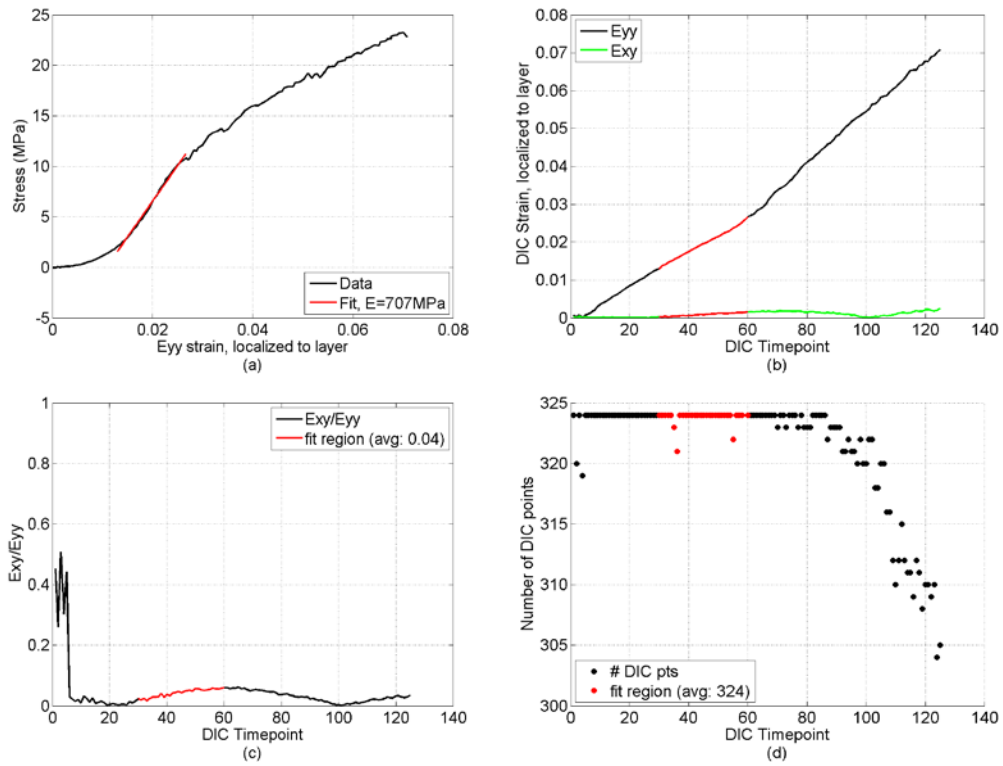

Fig. C-31 Specimen 02-15, layer from 80% to 90% depth

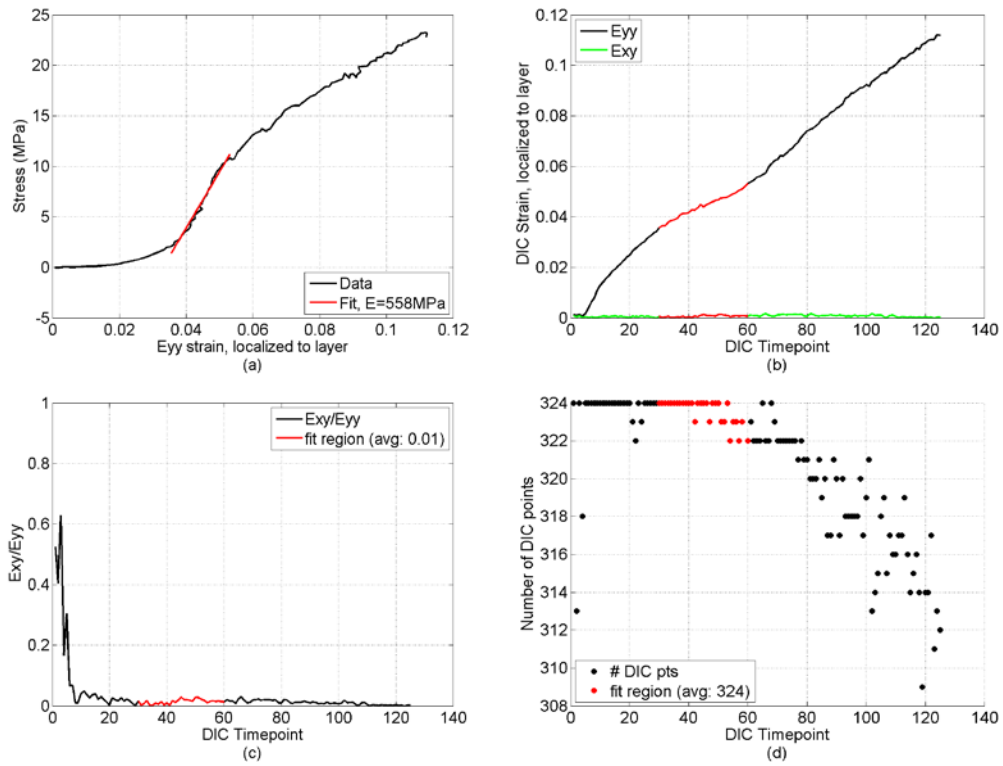

Fig. C-32 Specimen 02-15, layer from 90% to 100% depth

Lists of Symbols, Abbreviations, and Acronyms

E_0	tissue modulus of the bone material (BVF=100%)
E^n	apparent modulus (far-field) of layer *n*
μCT	micro-computed tomography
ρ_a	Apparent density, defined as the ratio of total mass to total volume of the specimen
ρ_b	Density of the bone tissue, defined as the ratio of total bone mass to the total bone volume
ARL	US Army Research Laboratory
BVF	bone volume fraction (in equations: f_{bv})
d	depth
DA	degree of anisotropy
DIC	digital image correlation
DVC	digital volume correlation
HBSS	Hank's Balanced Salt Solution
l	length
MIL	mean intercept length
ROE	region of extraction
TBI	traumatic brain injury
VOI	volume of interest
w	width
2-D	2-dimensional
3-D	3-dimensional

1 (PDF) DEFENSE TECHNICAL INFORMATION CTR DTIC OCA

2 (PDF) DIRECTOR US ARMY RESEARCH LAB RDRL CIO L IMAL HRA MAIL & RECORDS MGMT

1 (PDF) GOVT PRINTG OFC A MALHOTRA

1 (PDF) 1 MTRL SCIENCES DIV LAWRENCE BERKELY NATL LAB R RITCHIE

1 (PDF) BIOENGINEERING DEPT UNIV OF PENNSYLVANIA SCHOOL OF ENGRNG AND APPLIED SCIENCE S MARGULIES

1 (PDF) DEPT OF ENGRNG SCI AND MECHANICS VIRGINIA POLYTECHNIC INST AND STATE UNIV R BATRA

3 (PDF) MASSACHUSETTS INST OF TECHLGY INST FOR SOLDIER NANOTECHNOLOGIES B FAGAN R RADOVITZKY S SOCRATE

1 (PDF) DEPT OF MECHL AND NUCLEAR ENGRNG THE PENNSYLVANIA STATE UNIV R KRAFT

1 (PDF) WHITING SCHOOL OF ENGRNG JOHNS HOPKINS UNIV V NGUYEN

2 (PDF) SANDIA NATL LABS B SANBORN B SONG

74 (PDF) DIR USARL
RDRL CI
P PLOSTINS
RDRL CIH C
E CHIN
RDRL SLB W
P GILLICH
J GURGANUS
J IVANCIK
W MERMAGEN
K RAFAELS
RDRL WM
A RAWLETT
J LA SCALA
B FORCH
S KARNA
J MCCAULEY
S SCHOENFELD
RDRL WML
W OBERLE
RDRL WML F
G BROWN
RDRL WML G
J SOUTH
RDRL WML H
T EHLERS
L MAGNESS
C MEYER
J NEWILL
D SCHEFFLER
B SCHUSTER
RDRL WMM
J BEATTY
B DOWDING
RDRL WMM A
J GARDNER
D O'BRIEN
T PLAISTED
E WETZEL
RDRL WMM B
G GAZONAS
D GRAY
R KASTE
B LOVE
P MOY
T WALTER
V WU
C YEN
RDRL WMM C
A BUJANDA
R JENSEN
RDRL WMM D
R CARTER
B CHEESEMAN
J SIETINS
S WALSH

W ZIEGLER
RDRL WMM E
G GILDE
J LASALVIA
P PATEL
J SINGH
J SWAB
RDRL WMM F
S GRENDAHL
L KECSKES
RDRL WMM G
J LENHART
K MASSER
R MROZEK
K STRAWHECKER
RDRL WMP A
S BILYK
RDRL WMP B
S ALEXANDER
A DAGRO
A DILEONARDI
A EIDSMORE
A GUNNARSSON
C HOPPEL
Y HUANG
M KLEINBERGER
S SATAPATHY
A SOKOLOW
M SCHEIDLER
K THOMPSON
T WEERASOORIYA
S WOZNIAK
T ZHANG
RDRL WMP C
R BECKER
T BJERKE
J BRADLEY
D CASEM

INTENTIONALLY LEFT BLANK.